




Reverse Faulting Within a Continental Plate Boundary Transform System

Kirk F. Townsend¹ , Marin K. Clark¹ , and Nathan A. Niemi¹ 

¹Department of Earth and Environmental Sciences, University of Michigan, Ann Arbor, MI, USA

Key Points:

- Apatite and zircon helium thermochronometry data from the Western Transverse Ranges (WTR) yield late-Miocene through Pleistocene cooling ages
- Reverse faulting within the block initiated prior to, and propagates toward, the Big Bend restraining bend in the San Andreas fault
- Rapid post-late-Miocene tectonic exhumation in the region surrounding the Big Bend is localized within the WTR

Supporting Information:

Supporting Information may be found in the online version of this article.

Correspondence to:

K. F. Townsend,
kirkft@umich.edu

Citation:

Townsend, K. F., Clark, M. K., & Niemi, N. A. (2021). Reverse faulting within a continental plate boundary transform system. *Tectonics*, *40*, e2021TC006916. <https://doi.org/10.1029/2021TC006916>

Received 26 MAY 2021

Accepted 24 SEP 2021

Abstract Contractional deformation is common along transform plate margins where plate motion is oblique to the plate boundary. While faults that accommodate this deformation are often inferred to be subsidiary to the main plate boundary fault, we typically lack direct geometric or kinematic information. Here we investigate the timing of faulting relative to changes in the orientation of the North American-Pacific plate boundary. Coeval with development of an oblique plate boundary segment (i.e., the “Big Bend” of the San Andreas fault), active shortening is inferred to have initiated at ~5 Ma in the Western Transverse Ranges (WTR). However, new low-temperature thermochronometric data yield Miocene to Pleistocene apatite (U-Th-Sm)/He cooling ages and partially reset zircon (U-Th)/He ages. Inverse thermal modeling indicate that reverse faulting initiated as early as 10 Ma, several million years prior to our current understanding of the timing of the Big Bend. Reverse faults in the WTR also propagate from west to east, toward the San Andreas Fault, rather than outwards from it. New and existing thermochronometry data delineate the WTR as the locus of rapid post-Miocene exhumation, and demonstrate that similar exhumation is not present in the broader region surrounding the Big Bend. We posit that reverse faulting is localized in the WTR because of a weak underlying lithosphere and predates the more recent geometric anomaly of the restraining bend in the transform margin.

1. Introduction

Continental transforms are characterized by complex fault systems in which the geometry and location of the active plate boundary fault evolves rapidly in geologic time (e.g., 3–10 Myr; Crowell, 1979; Şengör et al., 2005; Walcott, 1998). Such plate boundary faults are often associated with subsidiary fault systems that are inferred to be related to compressional or extensional bends that evolve along the active plate boundary (Armijo et al., 2002; Dewey et al., 1998; Niemi et al., 2013; Spotila et al., 2001; Teyssier et al., 1995), or to the initiation and propagation of a new strand of the plate boundary fault (Armijo et al., 1999; Collett et al., 2019; Cowan et al., 1996; Little & Jones, 1998; Rohr, 2015; Wallace et al., 2012). As well, fault systems subsidiary to major continental transforms are often significant seismic hazards in their own right, amplifying regional seismic risk near plate boundaries and underscoring the need to better understand their structural relationships within plate boundary systems (Davis & Namson, 1994; Dolan et al., 1995; Duffy et al., 2013; Quigley et al., 2012).

The relationships between oblique plate boundary faults and associated subsidiary dip-slip fault systems have been explored with numerical models and physical experiments (Cooke et al., 2020; Hatem et al., 2015, 2017; Madden et al., 2017; McBeck et al., 2016, 2017), as well as in natural systems (e.g., Cunningham & Mann, 2007; Woodcock, 1986). Restraining and releasing bends in continental transforms are associated with localized compression or extension (Dewey et al., 1998; Teyssier et al., 1995), and both analog models and natural systems suggest a geometric and kinematic link between primary plate boundary transforms and subsidiary reverse or normal faults. Subsidiary faults typically interact with the plate boundary fault via compressional or extensional “flower structures” that join the main and subsidiary structures at depth (Cooke et al., 2013; Hatem et al., 2015; Niemi et al., 2013; Woodcock & Fischer, 1986), and in which the partitioning of subsidiary deformation into contractional (extensional) and strike-slip components is largely governed by the obliquity of plate motion to the orientation of the transform fault (e.g., Cunningham & Mann, 2007; Spotila et al., 2007). Such a geometric and kinematic relationship implies that the initiation of reverse (normal) faults near restraining (releasing) bends in plate boundary transforms is driven by the geometry of the fault bend, with subsidiary faults initiating either during or subsequent to development of the bend itself (Crowell, 1979).

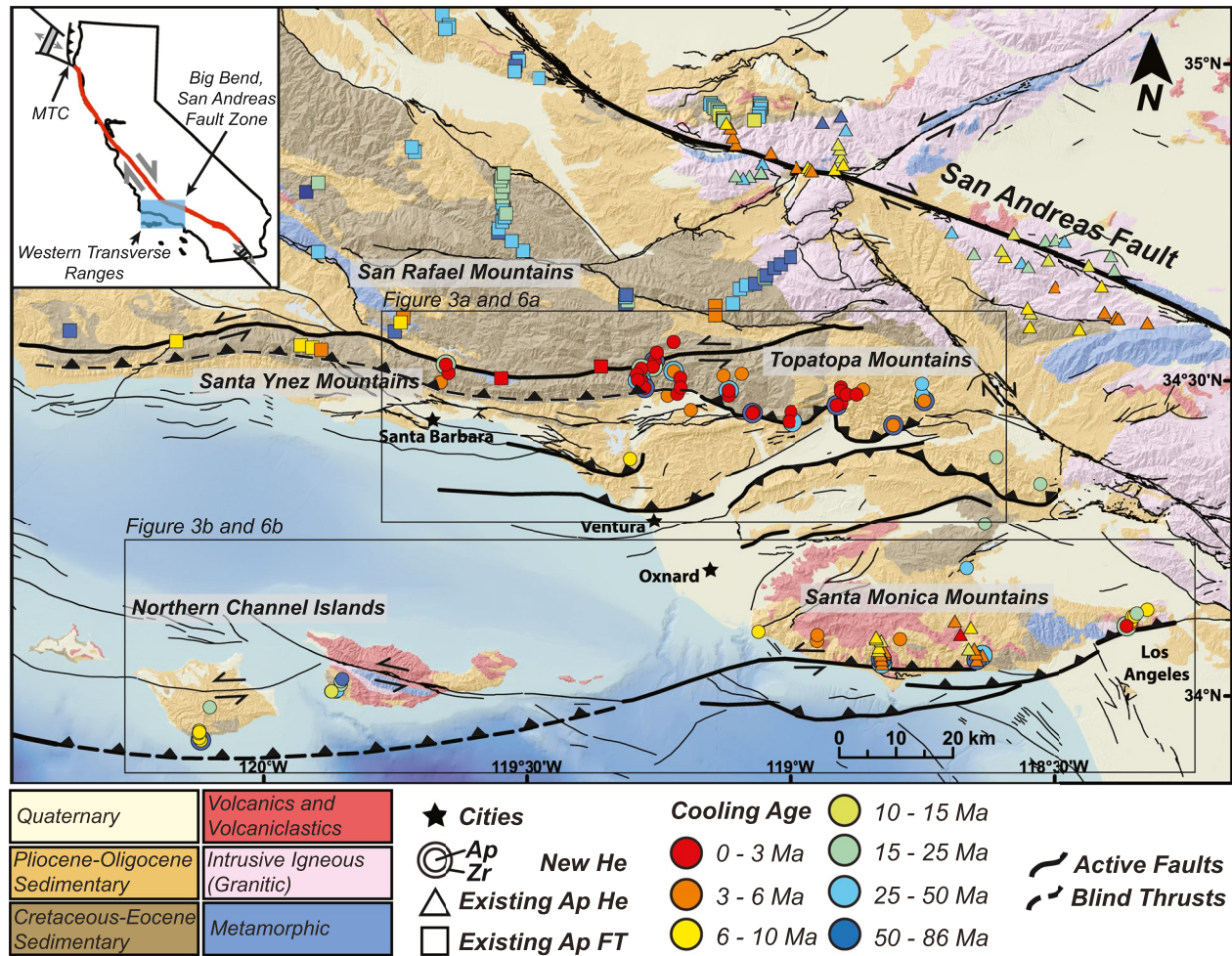


Figure 1. Simplified geology and structure of the Western Transverse Ranges (WTR) with sample locations. New apatite (U-Th-Sm)/He (AHe) samples are shown by small circles with a concentric larger circle where paired with zircon (U-Th)/He ages. Previously published AHe are shown by small rectangles (Buscher & Spotila, 2007; Niemi et al., 2013; Niemi & Clark, 2018), and previously published apatite fission track (AFT) are shown by small squares (Niemi et al., 2013; White, 1992). Faults with heavy line weights are the primary structures within the WTR.

The initiation of subsidiary fault systems with respect to the establishment of a plate boundary fault, and linkages between the growth and propagation of the plate boundary fault and subsidiary fault systems are not well documented from field studies, and there are clear examples where the geometry and kinematics of subsidiary dip-slip fault systems do not conform to the expectations of analog models, numerical simulations, and observations in some natural systems. The Western Transverse Ranges (WTR) of southern California, USA are hypothesized to be one such example. The WTR are an ~200 km by 70 km area of mountain ranges in southern California bounded by east-west oriented oblique-reverse faults (Figure 1). The major structures in the WTR are in close proximity to the ~160-km long restraining bend (i.e., the Big Bend) of the San Andreas Fault Zone within the continental transform boundary between the Pacific and North American plates (Atwater, 1998; Crowell, 1979; Huftile & Yeats, 1996; Jackson & Molnar, 1990; Luyendyk, 1991; Namson & Davis, 1988; Nicholson et al., 1994; Yeats, 1981). However, the geometry, extent, and kinematics of the faults in the WTR are hypothesized to be inconsistent with a mechanical linkage between subsidiary and primary plate boundary fault systems, as commonly described (e.g., Cunningham & Mann, 2007; Woodcock, 1986). The hypothesis of mechanical linkage between the WTR and the Big Bend remains untested, as the timing of dip-slip fault initiation in the WTR relative to the development of the Big Bend in the San Andreas Fault Zone has not been directly constrained.

Development of the Big Bend is constrained by fossil assemblages to ~5 Ma (Crowell, 1982; Link, 1982). Due to the close proximity of the WTR, as well as the structural implications of an adjacent transpressive bend, the timing of reverse fault initiation within the WTR is generally inferred to be at around the same time (Crowell, 1979). Independent timing of the initiation of reverse faulting in the WTR is currently poorly constrained by stratigraphic data (DeVecchio et al., 2012; Huftile & Yeats, 1996; Levi & Yeats, 1993; Yeats, 1993), and consequently, the kinematic relationship between the San Andreas Fault and the WTR has not been explicitly tested. An unexplored, but reasonable hypothesis, is that dip-slip structures in the WTR initiated independently within the diffuse Pacific-North American plate boundary zone, as a manifestation of inherited structural heterogeneities, rheologic contrasts, or other forcings (e.g., Woodcock, 1986).

The San Andreas fault is the archetypal continental transform system, and understanding the temporal and geometric relationships between the evolution of the Big Bend and the WTR is likely to lead to kinematic models that can be exported beyond western North America (e.g., the Marlborough Fault System of New Zealand, the North Anatolian Fault system of Turkey, and the Queen Charlotte Fault system offshore western Canada and Alaska). High resolution thermochronometric data can potentially discriminate between end member scenarios in which contractional structures in the WTR evolved synchronously with the Big Bend in the San Andreas Fault, or were kinematically “advected” into this restraining bend, and can therefore provide insight into the relationship between the reverse faults within the WTR and the evolution of California’s transform plate boundary. Here we present new apatite and zircon (U-Th-[Sm])/He thermochronometry data from the northern and southern boundaries of the WTR, where structural relief is greatest and reverse faulting is inferred to have initiated earliest. Samples from nine new transects and two published transects (Niemi & Clark, 2018) reveal predominantly Pliocene to Pleistocene apatite cooling ages in the Santa Ynez and Topatopa Mountains on the northern boundary, and latest-Miocene to Pliocene cooling ages in the Santa Monica Mountains and northern Channel Islands on the southern boundary (Figure 1). These data suggest recent and rapid rock exhumation, and inverse thermal modeling for time-temperature histories yield constraints on the timing of cooling and inferred reverse faulting. We also evaluate our thermochronometric results from samples collected both on and off of our main transects with respect to published thermochronometric ages (Buscher & Spotila, 2007; Niemi et al., 2013; White, 1992) from the broader region around the Big Bend in the San Andreas Fault to identify spatial trends in the localization of post-Miocene rapid exhumation.

2. Geologic Background

The WTR have experienced a complex history of extension, vertical-axis rotation, and shortening (Atwater, 1998). Forearc strata within the WTR were deposited on the margin of the North American plate above the subducting Farallon Plate in Cretaceous through Oligocene time, and the WTR were subsequently rifted from the continent and rotated following complete subduction of the Farallon Plate (Atwater, 1998; Crowell, 1979). The WTR underwent over 90° of clockwise vertical-axis rotation within the new diffuse transform margin between the Pacific and North American plates in Miocene time, and syn-rotation extension created deep, localized normal fault-bounded basins that filled with siliciclastic and volcanoclastic sedimentary strata (Atwater, 1998; Hornafius et al., 1986). The WTR are typically thought to have transitioned from extension to shortening following development of the Big Bend restraining bend in the San Andreas Fault at ~5 Ma (Crowell, 1979), but the timing of initiation of the principal reverse structures with the greatest structural relief remains unconstrained. Without dense, high-resolution data from the principal structures, the mechanistic relationship between the WTR and the San Andreas Fault Zone from Miocene-time to present remains unresolved.

2.1. Southern San Andreas Fault and the Big Bend

The San Andreas Fault system is the continental transform boundary between the Pacific and North American plates throughout much of California (Figures 1 and 2). Although the central San Andreas fault has largely remained in its current configuration since middle-Miocene time (Crowell, 1979; Graham et al., 1989), the southern section of the San Andreas Fault developed more recently at ~5 Ma (Crowell, 1982) (Figure 2). From about 12 to 5 Ma, the San Gabriel Fault linked directly with the San Andreas Fault to form the main plate boundary structure (Crowell, 1979; Ehlig et al., 1975). As slip progressed, the 11,000 m thick Violin

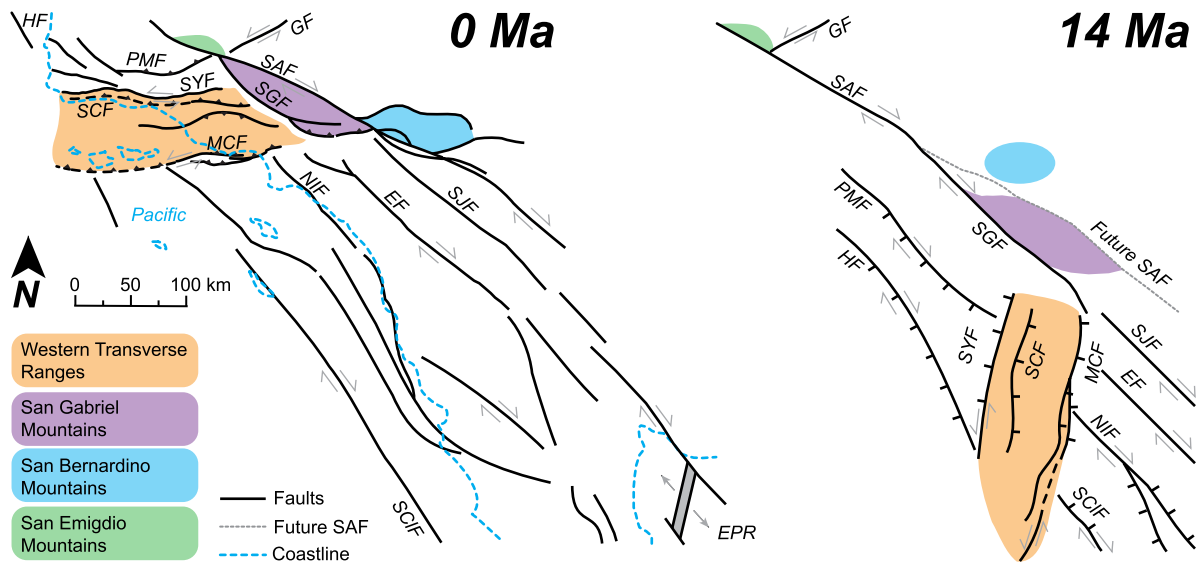


Figure 2. Present active faults in coastal southern California, USA, and Baja, Mexico (left) showing the locations of principal mountain ranges within the broader Transverse Ranges, including the San Gabriel Mountains, San Bernardino Mountains, San Emigdio Mountains, and the collective Western Transverse Ranges. With respect to the North American plate, the Western Transverse Ranges have undergone over 90° of clockwise rotation and translated northwest with the Pacific Plate since Middle-Miocene time (right) (Luyendyk, 1991; Nicholson et al., 1994). Prior to 5 Ma, the San Gabriel Fault was the principal plate boundary structure. Abandonment of this structure and development of the new southern San Andreas Fault to the east of the San Gabriel Mountains gave rise to the Big Bend restraining bend in the San Andreas Fault. EF, Elsinore Fault; EPR, East Pacific Rise; GF, Garlock Fault; HF, Hosgri Fault; MCF, Malibu Coast Fault; NIF, Newport Inglewood Fault; PMF, Pine Mountain Fault; SAF, San Andreas Fault; SCF, San Cayetano Fault; SCIF, San Clemente Fault; SGF, San Gabriel Fault; SJF, San Jacinto Fault; SYF, Santa Ynez Fault.

Breccia was deposited in a narrow basin directly adjacent to the fault zone within the broader Ridge Basin (Crowell, 1982; Link & Osborne, 1978). The deposition of the Hungry Valley Formation overtop both the Violin Breccia and the fault zone at ~5 Ma is interpreted to reflect the cessation of slip on the San Gabriel Fault and the abandonment of this structure as the principal trace of the North American-Pacific Plate boundary (Crowell, 1982; Link, 1982; Link & Osborne, 1978). The new southern San Andreas Fault formed to the east of the San Gabriel Fault, and connected with the central section of the San Andreas Fault to the north, creating the ~160 km restraining bend (i.e., the Big Bend) in the fault (Crowell, 1979) (Figure 2). Development of this structure is typically thought to have initiated regional shortening across the WTR, causing normal faults that were active within a transtensional stress field during Miocene time to re-activate as high-angle reverse faults in Pliocene time (Dolan et al., 1995; Hornafius et al., 1986; Huftile & Yeats, 1996; Wright, 1991). This transpressional stress state persists to the present time (Marshall et al., 2013, 2017).

2.2. Sedimentology and Rotation of the Western Transverse Ranges

The WTR are predominantly composed of a ~13 km thick section of late-Mesozoic through Cenozoic clastic sedimentary rocks and Miocene volcanic and volcanoclastic rocks that overlie continental plutonic and metamorphic basement in the east (locally exposed in the eastern Santa Monica Mountains), and oceanic ophiolitic-Franciscan basement complex in the west (exposed on Santa Cruz Island and the central Santa Ynez Mountains) (Dibblee, 1982; Namson & Davis, 1988). During Cretaceous and early Cenozoic time, the WTR accumulated sediments derived from the continent in the forearc above the subducting Farallon Plate (Atwater, 1998). Shallow-marine to terrestrial sandstones and conglomerates were deposited in Oligocene time as the Pacific Plate first made contact with the North American Plate and the boundary transitioned from subduction to predominantly transform (Crowell, 1979). During Miocene time, thick sections of marine siliceous mudstones, marine sandstones, and volcanoclastic rocks locally accumulated in extensional basins as the region underwent rotation and left-lateral shearing in a transtensional tectonic regime (Atwater, 1998; Namson & Davis, 1988; Nicholson et al., 1994; Wright, 1991).

Sedimentation across the WTR in Middle-Miocene time was associated with vertical-axis rotation of the region (Luyendyk, 1991; Sorensen, 1985). The WTR has undergone over 90° of clockwise rotation since ~15 Ma, as indicated by both geologic evidence (Crouch, 1979; Sorensen, 1985) and paleomagnetic data (Hornafius et al., 1986; Kamerling & Luyendyk, 1979, 1985; Luyendyk, 1991) (Figure 2). The WTR are thought to have rotated as a coherent block within a diffuse transform margin between the Pacific and North American plates, and are juxtaposed against non-rotated crust to the north and south (Hornafius et al., 1986; Luyendyk, 1991; Nicholson et al., 1994). A number of kinematic models have been proposed for this rotation. The most common mechanism posited invokes rotation along left-lateral strike-slip faults bounding the eastern and western margins of the WTR, with non-rotating blocks to the north and south (Luyendyk et al., 1980) (Figure 2). To address space problems in these kinematic models, the width of both the rotating block and the bounding shear zone are thought to have changed through time, with an initial period of extension followed by contraction (Dickinson, 1996; Luyendyk, 1991). Sedimentation in deep, localized basins in Miocene time record this initial phase of extension (Atwater, 1998; Namson & Davis, 1988; Nicholson et al., 1994), but geologic evidence for a subsequent phase of transpressional deformation prior to development of the Big Bend has yet to be documented.

2.3. Principal Fault Systems

The WTR can be broadly divided into two principal fault systems, which parallel one another and accommodate north-south contraction on east-west trending fault systems in the current geometry. Herein, we refer to these two principal fault systems as the San Cayetano and Santa Monica-Channel Islands fault systems, respectively.

2.3.1. San Cayetano Fault System

The San Cayetano fault system includes the Santa Ynez Fault and San Cayetano Fault, which bound the Santa Ynez and Topatopa Mountains on the northern boundary of the WTR (Figures 1 and 3a). The main structural feature of the Santa Ynez Mountains is the ~160-km long, east-west striking Santa Ynez anticlinorium, which has a predominantly overturned south limb and is composed of a 5-km thick section of Cretaceous, Eocene, and Oligocene strata (Dibblee, 1982). Although the Santa Ynez Fault bounds the range to the north, late-Quaternary motion on this structure is predominantly left-lateral strike-slip (Darrow & Sylvester, 1984), and the fault is considered too far north of the anticlinorium to have produced this structure (Levy et al., 2019). Likely, a blind extension of the San Cayetano Fault west of where surface displacement terminates in the Ojai Valley lies beneath the Santa Ynez Mountains and is responsible for most of the surface uplift and folding of the anticlinorium (Figure 3a) (Levy et al., 2019; Namson & Davis, 1988). The south-verging San Cayetano Fault becomes emergent in the easternmost Santa Ynez Mountains, where it cuts the south limb of the anticlinorium in a structurally complex series of plunging folds that form the boundary between the Santa Ynez and Topatopa Mountains (Rockwell, 1988). To the east, the Topatopa Mountains are largely composed of the same Eocene through Miocene strata as the Santa Ynez Mountains, but here these units generally strike north-south and dip gently off to the east (Figure 3a) (Dibblee, 1990a, 1990b, 1991c). The emergent portion of the San Cayetano Fault juxtaposes Eocene strata in the hanging wall against Quaternary sediments in the footwall with as much as 9 km of stratigraphic separation (Rockwell, 1988).

Recent work on the San Cayetano fault system suggests that these structures and associated folds have evolved as a classic forward-propagating fold and thrust belt (Hubbard et al., 2014; Levy et al., 2019). The blind portion of the San Cayetano Fault beneath the Santa Ynez Mountains is likely no longer active as deformation stepped southward beginning around ~1 Ma (Yerkes & Lee, 1987), first to the Red Mountain and South Sulphur Mountain faults, and most recently to the Ventura-Pitas Point fault system (Figure 3a) (Hubbard et al., 2014; Levy et al., 2019; Perea et al., 2017). These structures likely converge onto a mid-crustal décollement at depth, which has been interpreted to be a south-verging structure (Levy et al., 2019; Rockwell, 1983). Rupture of this thrust ramp may be responsible for the large (up to ~10 m) co-seismic surface uplift and fault displacements documented along the Ventura-Pitas Point fault system (Hubbard et al., 2014; Hughes et al., 2018; Levy et al., 2019; McAuliffe et al., 2015; Rockwell et al., 2016).

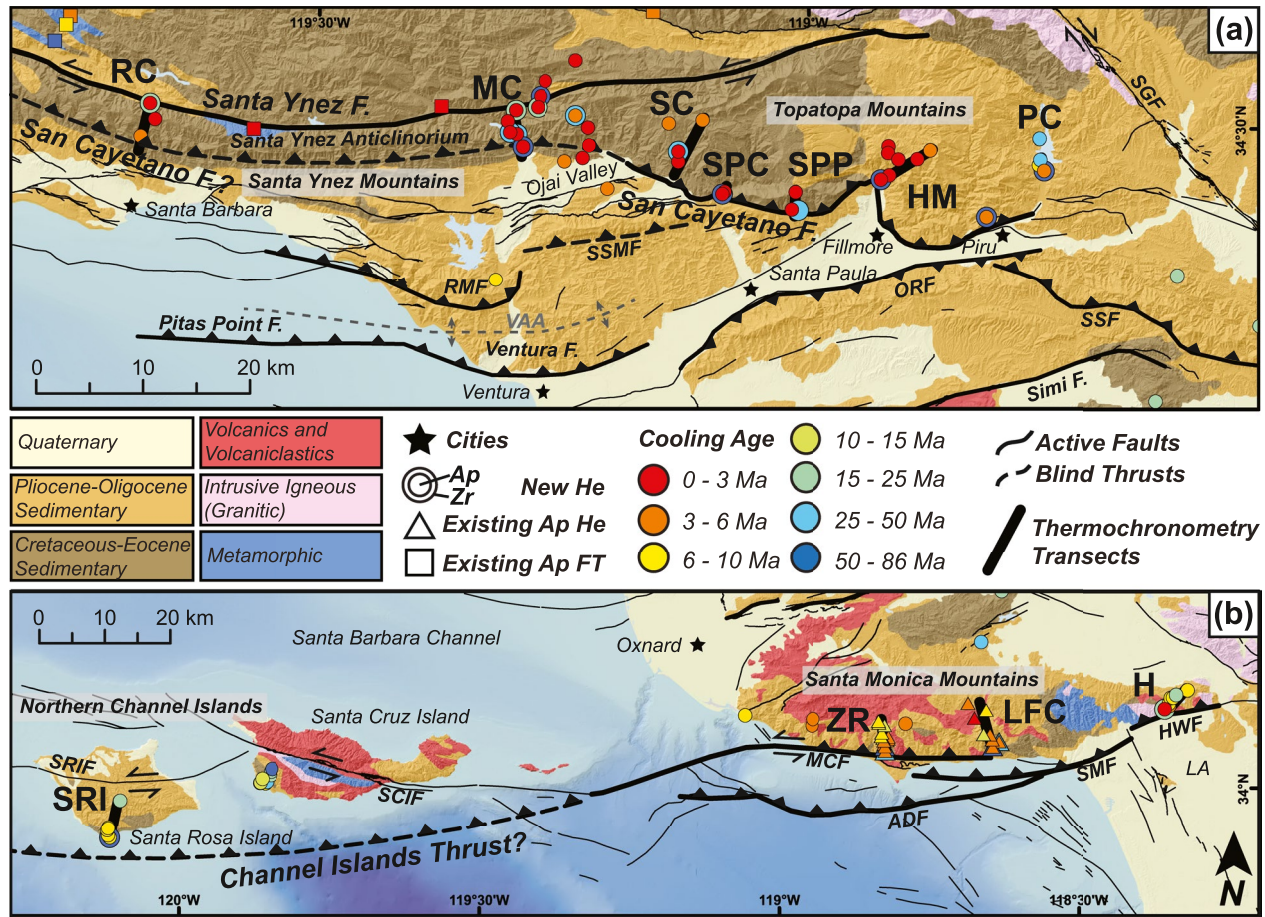


Figure 3. Bedrock geology and thermochronometry sample locations along (a) the San Cayetano fault system and (b) the Channel Islands-Santa Monica fault system in the Western Transverse Ranges. Transect labels: RC—Rattlesnake Canyon; MC—Matilija Canyon; SC—Sisar Canyon; SPC—Santa Paula Canyon; SPP—Santa Paula Peak; HM—Hopper Mountain; PC—Piru Canyon; SRI—Santa Rosa Island; ZR—Zuma Ridge (Niemi & Clark, 2018); LFC—Las Flores Canyon (Niemi & Clark, 2018); H—Hollywood. Fault abbreviations: ADF—Anacapa-Dume Fault; HWF—Hollywood Fault; MCF—Malibu Coast Fault; ORF—Oak Ridge Fault; RMF—Red Mountain Fault; SGF—San Gabriel Fault; SMF—Santa Monica Fault; SCIF—Santa Cruz Island Fault; SRIF—Santa Rosa Island Fault; SSF—Santa Susana Fault; SSMF—South Sulphur Mountain Fault; VAA—Ventura Avenue Anticline. F—Fault.

2.3.2. Santa Monica-Channel Islands Fault System

On the southern boundary of the WTR, the Santa Monica-Channel Islands fault system includes a series of south-verging reverse to left-lateral strike-slip faults (Figure 3b) (Davis & Namson, 1994; Dolan & Pratt, 1997; Dolan et al., 1997, 2000; Seeber & Sorlien, 2000; Shaw & Suppe, 1994). The Santa Monica Mountains and northern Channel Islands have been exhumed in the hanging wall of these structures and are generally composed of Cretaceous through Miocene marine sedimentary rocks and Miocene volcanoclastic units. The oldest rocks are exposed at the eastern end of the Santa Monica Mountains, where granitic basement and Jurassic metamorphic rocks (the Santa Monica Slate) are exposed in the hanging wall of the Santa Monica and Hollywood faults (Dibblee, 1991a, 1991b), and in the west on Santa Cruz Island, where Jurassic-age schist is exposed south of the Santa Cruz Island Fault (Hill, 1976). The Paleocene through late-Miocene strata generally dip gently to the north and are continuous along-strike for ~220 km from the central Santa Monica Mountains in the east through San Miguel Island in the west. The northward dip of the Paleocene through late-Miocene strata is likely a consequence of rotation in the hanging walls of the underlying north-dipping thrusts (Davis & Namson, 1994; Seeber & Sorlien, 2000; Shaw & Suppe, 1994; Sorlien et al., 2006). Progressive northward-tilting of the hanging walls of the north-dipping thrusts during Pliocene time suggests that these structures are listric (Pinter et al., 2001; Seeber & Sorlien, 2000).

3. Low-Temperature Thermochronometry Methods

Fault initiation and fault slip rates are commonly interpreted from low-temperature thermochronometry data. Ages from low-temperature thermochronometers are sensitive to tectonic and geomorphic processes affecting the upper few kilometers of the crust, and as such, are well suited for constraining the history of relatively young, brittle structures (Ehlers, 2005). Apatite (U-Th-Sm)/He ages (AHe) represent the time since a sample cooled below $\sim 40\text{--}80^\circ\text{C}$, depending on radiation damage, grain size, and cooling rate, which equates to 2–4 km depth for typical geothermal gradients (Farley, 2002; Flowers et al., 2009). Zircon (U-Th)/He (ZHe) ages record cooling below $\sim 180\text{--}200^\circ\text{C}$, or depths of 5–8 km (Farley, 2002; Reiners et al., 2002). Where samples are collected on vertical transects with respect to elevation or depth beneath a stratigraphic horizon, resultant gradients in age versus depth represent exhumation rates averaged over several million years (Farley, 2002). We targeted multiple vertical and stratigraphic transects for sampling along-strike of the principal fault zones (Figure 3). Collection of thermochronometry data from sedimentary rocks requires particular attention to the thermal history of individual mineral grains within the rock. Detrital grains commonly record an older thermal history related to the sedimentary source terrane, unless burial during sedimentation reaches a high enough temperature to reset the thermochronometer. Cooling ages that are younger than the depositional age of the sampled rock are assumed to be reset, and thus to record a thermal event related to the exhumation of the sedimentary rock. Conversely, cooling ages older than the depositional age of a sedimentary rock are inferred to be inherited from the source terrane from which the sedimentary rock was derived (Lock & Willett, 2008).

3.1. Apatite and Zircon (U-Th-[Sm])/He Methods

Samples were processed using standard methods to isolate apatite and zircon (Text S1 in Supporting Information S1). Individual mineral grains were hand-selected under a high-powered binocular microscope to screen for clarity, crystal morphology, and minimal inclusions of other potentially radiogenic minerals. All grains analyzed are $>80\ \mu\text{m}$ in both length and width. Helium outgassing was conducted on an Alphachron Helium Instrument at the University of Michigan following the procedures in Niemi and Clark (2018), and concentrations of U, Th, and Sm (apatite only) were measured using a Thermo Scientific Element 2 ICP-MS at the University of Arizona following the procedures in Reiners and Nicolescu (2006). Mean ages reported here are based on 3–10 individual replicate analyses for each sample. Individual grains were excluded from the calculation of mean ages and thermal models following the criteria of Niemi and Clark (2018) (Text S1 in Supporting Information S1).

3.2. Inverse Thermal Modeling Approach

We develop thermal histories using QTQt (Gallagher, 2012; Macintosh version 64R5.7.0), which inverts thermochronometry age data from multiple samples on vertical profiles simultaneously. Uncorrected grain ages, grain sizes, and concentrations of He, U, Th, and Sm (AHe only) were entered into QTQt for each apatite and zircon grain (Supporting Information S1). Models were run with a burn-in of 30,000 iterations and then sampled over 80,000 iterations with a thinning of 1. Grain age error resampling using a MCMC (Markov Chain Monte Carlo) was enabled to account for observed differences between analytical uncertainties in individual grain ages and reproducibility of ages (e.g., McDowell et al., 2005). Due to predominantly young cooling ages, no radiation damage model was used for apatite samples, however, the Guenther et al. (2013) radiation model was implemented for all zircon grains.

Thermal models were constrained by stratigraphic data and higher temperature thermochronometry. Typically, models were constrained to a time and temperature range of 0–110 Ma and 0–300°C, respectively. Depositional age constraints of samples from sedimentary rocks were inferred from stratigraphic ages on published geologic maps and used as depositional age constraints in the thermal models (Table 1; Dibblee, 1985, 1987a, 1987b, 1990a, 1990b, 1991a, 1991b; Dibblee & Ehrenspeck, 1986, 1997; Dibblee et al., 1998). We did not impose burial depth constraints on samples. A crystallization age for the two samples collected from the pluton at the base of the Hollywood transect is constrained by a hornblende K/Ar age of 105 ± 3.2 Ma (Miller & Morton, 1980). Fission track length and count data from a single apatite sample (WG2-90) from White (1992) was included in the Matilija Canyon transect thermal model. WG2-90

Table 1
Thermochronometry Data Used in Inverse Thermal Modeling

Sample name	Longitude (degrees)	Latitude (degrees)	Elevation (m)	Modeled stratigraphic position (m)	Geologic formation	Age of formation	Mean apatite He age (Ma)	Mean zircon He age (Ma)
Rattlesnake Canyon transect (RC)								
18-SBRC-03	-119.6805	34.4745	763	1,222	Cozy Dell Shale	Late-Eocene	3.8 ± 0.3	
18-SBRC-05	-119.6660	34.4892	1,113	641	Juncal	Early- to Middle-Eocene	3.0 ± 0.1	
18-SBRC-07	-119.6715	34.5025	693	35	Unnamed Marine	Cretaceous	2.0 ± 0.1	15.3 ± 0.6
Matilija Canyon Transect (MC)								
16-OJ-01	-119.2897	34.4737	280	2,428	Coldwater Sandstone	Late-Eocene	2.9 ± 0.3	52.0–71.4 ^a
16-OJ-02	-119.3033	34.4855	315	1,493	Matilija Sandstone	Middle- to Late-Eocene	2.0 ± 0.03	34.3 ± 3.8
17-OJ-06	-119.2753	34.5072	540	428	Unnamed Marine	Cretaceous	1.6 ± 0.2	10.3–36.3 ^b
17-OJ-07	-119.2974	34.5040	418	901	Juncal	Early- to Middle-Eocene	1.95 ± 0.53	17.7 ± 3.1
17-OJ-08	-119.3058	34.4946	368	1,072	Juncal	Early- to Middle-Eocene	1.5–2.1 ^c	
17-OJ-09	-119.2964	34.4839	282	1,892	Cozy Dell Shale	Late-Eocene	2.0 ± 0.1	35.3 ± 0.7
Sisar Canyon Transect (SC)								
18-OSC-03	-119.1298	34.4641	723		Matilija Sandstone	Middle- to Late-Eocene	2.1 ± 0.1	
18-OSC-05	-119.1302	34.4725	1,085		Juncal	Early- to Middle-Eocene	2.7 ± 0.2	11.8–40.5 ^d
18-OSC-07	-119.1059	34.4993	1,928		Juncal	Early- to Middle-Eocene	3.3 ± 0.2	
18-OSC-10	-119.1405	34.4959	1,606		Matilija Sandstone	Middle- to Late-Eocene	3.4 ± 0.02	
Santa Paula Canyon (SPC)								
16-SP-03	-119.0843	34.4375	342		Coldwater Sandstone	Late-Eocene	2.1 ± 0.1	56.3 ± 8.8
Santa Paula Peak (SPP)								
18-SPP-02	-119.0134	34.4254	760		Matilija Sandstone	Middle- to Late-Eocene	1.3 ± 0.2	
18-SPP-03	-119.0097	34.4403	1,512		Matilija Sandstone	Middle- to Late-Eocene	2.7 ± 0.3	
18-SPP-06	-119.0068	34.4248	936		Matilija Sandstone	Middle- to Late-Eocene		50.0 ± 7.8
Hopper Mountain Transect (HM)								
16-FM-01	-118.9218	34.4522	264		Sespe	Oligocene	1.7 ± 0.1	53.2–72.0 ^a
17-FC-01	-118.9133	34.4560	353		Vaqueros Sandstone	Oligocene to Early-Miocene	1.6 ± 0.2	
17-FC-02	-118.9148	34.4804	756		Sespe	Oligocene	1.9 ± 0.4	
17-FC-03	-118.9149	34.4750	671		Sespe	Oligocene	1.7 ± 0.1	
17-FC-04	-118.9042	34.4695	552		Vaqueros Sandstone	Oligocene to Early-Miocene	1.8 ± 0.2	
18-FC-01	-118.8722	34.4778	1,263		Monterey	Middle- to Late-Miocene	3.3 ± 0.3	
18-FC-02	-118.8849	34.4702	1,142		Monterey	Middle- to Late-Miocene	1.9 ± 0.2	
Santa Rosa Island Transect (SRI)								
18-SRI-05	-120.1220	33.9123	249	874	Glendora Volcanics	Early-Miocene	8.6 ± 1.3	
18-SRI-06	-120.1188	33.8975	160	283	South Point Sandstone	Middle-Eocene	6.4 ± 0.1	51.3–85.0 ^a
18-SRI-07	-120.1214	33.9005	163	397	Sespe	Oligocene	8.4 ± 0.9	
18-SRI-10	-120.1217	33.9103	247	647	Sespe	Oligocene	7.6 ± 0.5	
Hollywood Transect (H)								
16-NC-01	-118.3612	34.1083	176	1	Granitic Rocks	Cretaceous	3.0 ± 0.1	22.1 ± 1.5
17-HW-01	-118.3510	34.1236	292	1,755	Middle Topanga	Middle-Miocene	7.1 ± 0.8 ^e	
17-HW-02	-118.3471	34.1246	289	1,980	Upper Topanga	Middle-Miocene	8.5 – 8.7 ^{e,c}	
17-HW-03	-118.3533	34.1127	357	855	Granitic Rocks	Cretaceous	4.6 ± 0.2	
17-HW-04	-118.3537	34.1157	378	1,020	Unnamed Strata	Cretaceous	8.6 ± 1.3	

Table 1
Continued

Sample name	Longitude (degrees)	Latitude (degrees)	Elevation (m)	Modeled stratigraphic position (m)	Geologic formation	Age of formation	Mean apatite He age (Ma)	Mean zircon He age (Ma)
17-HW-06	-118.3232	34.1346	511	2,476	Upper Topanga	Middle-Miocene	8.7 ± 1.6 ^e	

Note. We exclude grains with uranium concentrations under 5 ppm from thermal models and calculation of mean ages. Outliers were identified using the Q-test at the 90% confidence interval. We consider samples with a standard error greater than 1.0 Ma that is also greater than 20% of the mean age to have low reproducibility, and report ranges of individual grain ages instead of mean ages. We also report ranges of individual grain ages instead of mean ages for samples with grain ages that are older than the depositional age of the sedimentary rock from which they were collected as these ages are likely inherited and do not reflect recent cooling of the sample.

^aMean cooling age is older than the depositional age of the sedimentary rock. Range of grain ages reported instead of mean age. Grains not used in thermal modeling. ^bStandard error is >20% of mean age. Range of grain ages reported instead of mean age. ^cFewer than three grains analyzed or remaining after rejecting outliers and low-U grains. Range of grain ages reported instead of mean age. ^dStandard error is >20% of mean age, and two of four grain ages are the same as the depositional age of the sedimentary rock. Range of grain ages reported instead of mean age. Grains not used in thermal modeling. ^eMean cooling age is within the depositional age of the sampled strata. Not used in inverse modeling, but predicted cooling histories and ages are included.

track length and count data were included in the QTQt input file for sample 17-OJ-07, which was collected from the same outcrop.

For each thermal model, the geothermal gradient was set to the range $30 \pm 5^\circ\text{C}$. This range is consistent with modern geothermal gradients measured in boreholes within the WTR (Bostick et al., 1978; Nathenson Marianne, 1987), as well as maximum paleo-geothermal gradients inferred from vitrinite reflectance data from Miocene through Pliocene sedimentary rocks in the Ventura Basin (Bostick et al., 1978) and the Cretaceous through Eocene section in the Santa Ynez Mountains (Helmold & van de Kamp, 1984). The agreement between modern and paleo-geothermal data suggests that the Cenozoic section in the WTR has not been subject to a higher geothermal gradient than is measured today, so we assume that the modern geothermal gradient is representative of the geothermal gradient during the last few million years. We define a present-day surface temperature of $12 \pm 5^\circ\text{C}$ in each thermal model, and we assume that all samples were at the surface ($5 \pm 5^\circ\text{C}$) at the time of deposition (Niemi & Clark, 2018). The present-day temperature difference between the highest and lowest samples on each transect was set to a typical atmospheric lapse rate of $6 \pm 2^\circ\text{C}/\text{km}$ (Stone & Carlson, 1979).

The spatial relationship of individual samples within the thermal field through which they cooled can be used in a model to derive exhumation rates from cooling rates. Typically, elevation or stratigraphic depth are used. Here, we defined vertical separation of individual samples in thermal models using stratigraphic separation between samples as derived from cross sections constructed from published geologic maps (Figures S1–S3 in Supporting Information S1; Dibblee, 1985, 1987a, 1987b, 1991a; Dibblee & Ehrenspeck, 1986; Dibblee et al., 1998). Where the stratigraphic separation was unclear or minimal, samples were modeled with vertical separation defined by present-day elevations above sea level (Figure 4).

4. Apatite and Zircon Age Data

New helium thermochronometry data are presented for seven transects in the Santa Ynez Mountains and Topatopa Mountains on the San Cayetano fault system, and two transects on the Santa Monica-Channel Islands fault system (Figures 1 and 3, Tables 1 and 2; Supporting Information S1). Sixty-seven apatite ages were produced, for which 16 samples also have ZHe data. Age and thermal modeling results from two transects in the central Santa Monica Mountains (Niemi & Clark, 2018) are also interpreted in a regional context here. All samples were collected from the hanging walls of reverse faults that bound the principal ranges. Additional samples were collected off the main transects to identify the spatial distribution of young cooling ages (Figures 1 and 3, Table 2).

Pliocene to early Quaternary AHe ages from samples collected from Oligocene-Cretaceous sedimentary strata indicate that most samples are thermally reset and record recent exhumation of fault bounded ranges (Table 1). Reset AHe ages from the San Cayetano fault system transects range from 1.3 to 5.9 Ma, and AHe ages from the Santa Monica-Channel Islands fault system transects range from 2.6 to 8.6 Ma. Notably

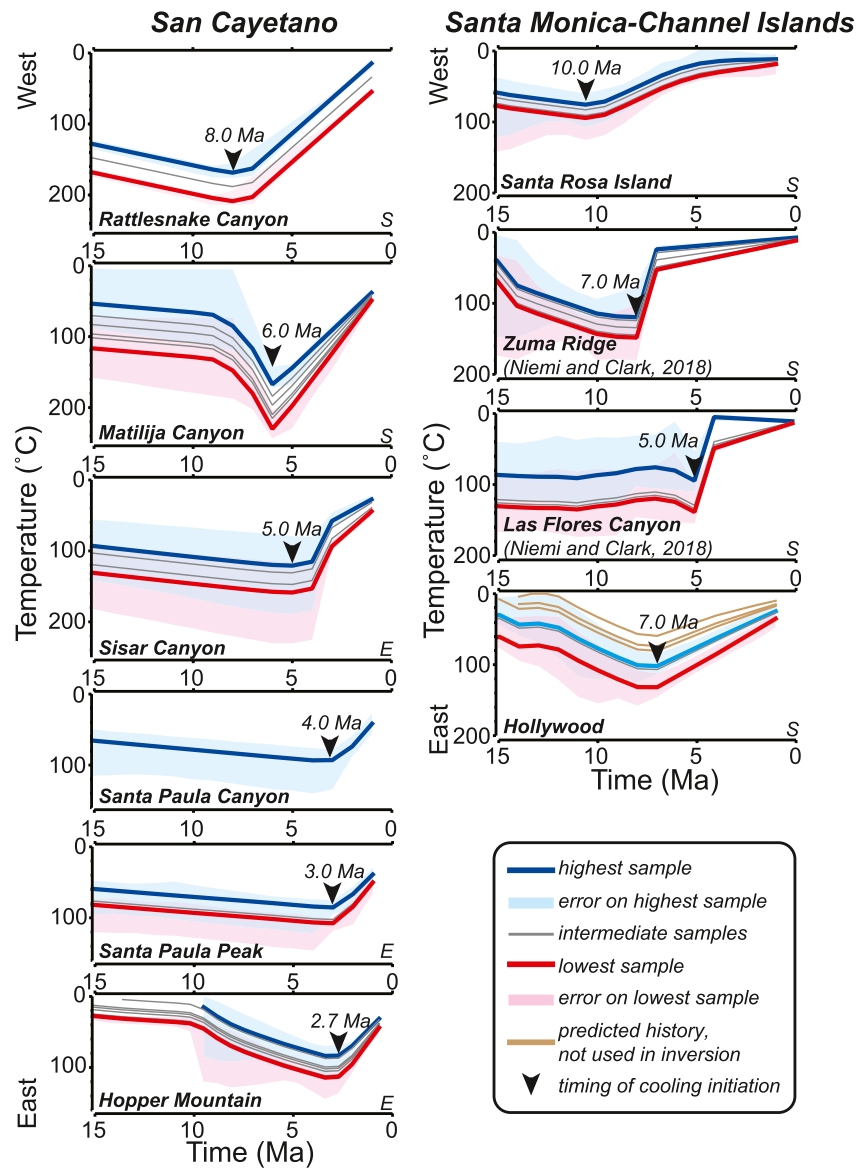


Figure 4. Inverse models of best-fit thermal histories for the last 15 Ma. Thermal history models from transects on both the San Cayetano and Santa Monica-Channel Islands fault systems are arranged from west (top) to east (bottom) (see Supporting Information S1 for full thermal histories). Black arrows show timing of cooling initiation. Samples were buried between Cretaceous and late Miocene time, and have been exhumed since early Pliocene time from temperatures of 100°C–220°C. Predicted thermal histories for three samples collected from Miocene strata on the Hollywood transect are shown, but these samples were not used in the inversion. See Table 1 for samples included in each model. S—vertical sample separation defined by stratigraphic separation; E—vertical sample separation defined by elevation.

however, AHe samples are reset only in Oligocene and older strata (Tables 1 and 2). Samples from Miocene strata yield variable AHe cooling ages, with individual grain ages ranging from 1.4 to 79 Ma. Five Miocene samples yield replicate ages with poor grain reproducibility, and eight Miocene samples yield cooling ages that are older than the depositional age of the sampled strata, suggesting that Miocene and younger strata were not buried deeply enough to fully reset the apatite helium thermochronometer. These non-reset ages indicate that burial of the sampled locations cannot have exceeded ~2 km, assuming typical geothermal gradients (e.g., Townsend et al., 2020). The non-reset ages therefore provide an upper limit on the magnitude of recent exhumation of <2 km. Non-reset AHe ages were not included in thermal models.

Table 2
Thermochronometry Data Not Used in Inverse Thermal Modeling

Sample name	Longitude (degrees)	Latitude (degrees)	Elevation (m)	Geologic formation	Age of formation	Mean apatite He age (Ma)	Mean zircon He age (Ma)
Matilija Canyon							
17-OJ-05	-119.2722	34.5166	586	Coldwater Sandstone	Late-Eocene	2.7 ± 0.3	49.4–62.9 ^{a,b}
Gridley Canyon							
17-GC-02	-119.2357	34.5008	1,253	Juncal	Early- to Middle-Eocene	3.3 ± 0.1	26.3 ± 3.5
17-GC-05	-119.2227	34.4908	763	Juncal	Early- to Middle-Eocene	2.8 ± 0.2	
17-GC-07	-119.2215	34.4757	482	Cozy Dell Shale	Late-Eocene	2.4 ± 0.3	
17-GC-08	-119.2276	34.4652	309	Coldwater Sandstone	Late-Eocene	2.6 ± 0.2	
17-GC-09	-119.2459	34.4621	295	Sespe	Oligocene	3.6 ± 0.6	
Ojai Valley							
17-OJ-01	-119.2017	34.4398	368	Sespe	Oligocene	5.0 ± 0.8	
17-OJ-03	-119.2681	34.5293	801	Cozy Dell Shale	Late-Eocene	2.3 ± 0.2	
17-OJ-04	-119.2370	34.5473	1,094	Matilija Sandstone	Middle- to Late-Eocene	2.7 ± 0.5	
17-VC-01	-119.3145	34.3604	79	Sespe	Oligocene	2.4 – 9.2 ^b	
Santa Paula Canyon							
16-SP-01	-119.0821	34.4393	356	Cozy Dell Shale	Late-Eocene	2.3 ± 0.2	
Piru Canyon							
16-PC-01	-118.7612	34.4670	344	Monterey	Middle- to Late-Miocene	4.8 – 24.3 ^b	
16-PC-02	-118.8137	34.4223	333	Monterey	Middle- to Late-Miocene	5.9 ± 1.0	75.2 – 89.4 ^a
16-PC-03	-118.7597	34.4715	346	Monterey	Middle- to Late-Miocene	20.5 – 48.7 ^{a,b}	
16-PC-04	-118.7557	34.4622	365	Monterey	Middle- to Late-Miocene	2.8 – 27.0 ^b	63.7 – 86.3 ^a
16-PC-06	-118.7607	34.4889	341	Monterey	Middle- to Late-Miocene	- ^c	
Santa Susana Mountains							
14-Sy-01	-118.5328	34.3334	760	Towsley	Late-Miocene	14.4 – 35.3 ^{a,d}	
14-Sy-02	-118.6173	34.3746	525	Towsley	Late-Miocene	14.0 – 24.8 ^{a,d}	
Simi Hills							
17-ESC-01b	-118.6701	34.1972	354	Detrital Sediments of Lindero Canyon	Middle Miocene	22.3–43.7 ^a	
17-RP-01	-118.6372	34.2686	501	Chatsworth	Late-Cretaceous	17.4 ± 1.0	
Santa Rosa Island							
18-SRI-02	-120.1036	33.9500	467	Rincon Formation	Early-Miocene	12.0 – 34.3 ^a	
18-SRI-09	-120.1229	33.9081	297	South Point Sandstone	Middle-Eocene	7.6 ± 0.4	
Santa Cruz Island							
18-PS-01	-119.8720	33.9804	7	Beechers Bay	Middle-Miocene	21.9 – 31.9 ^a	
18-PS-03	-119.8626	33.9802	15	Vaqueros	Early-Miocene	7.0 ± 0.6	
18-PS-04	-119.8604	33.9822	23	Jolla Viejo	Middle-Eocene	29.5 ± 2.7	
18-PS-05	-119.8539	33.9917	65	Canada	Middle- to Late-Eocene	18.2 ± 2.3	
18-PS-06	-119.8542	33.9966	195	Pozo	Paleocene	22.5 ± 0.4	
18-PS-07	-119.8519	34.0005	288	Rincon	Early-Miocene	10.4 – 79.2 ^a	
18-PS-08	-119.8710	33.9807	15	San Onofre Breccia	Early-Miocene	14.3 ± 0.9	
Central and Western Santa Monica Mountains							
16-SM-02	-118.7939	34.0830	547	Lower Topanga	Early- to Middle-Miocene	2.2 – 6.3 ^b	
16-YB-01	-118.9510	34.0777	219	Lower Topanga	Early- to Middle-Miocene	5.2 ± 0.2	
16-YB-02	-118.9501	34.0868	304	Lower Topanga	Early- to Middle-Miocene	4.2 ± 0.8	

Table 2
Continued

Sample name	Longitude (degrees)	Latitude (degrees)	Elevation (m)	Geologic formation	Age of formation	Mean apatite He age (Ma)	Mean zircon He age (Ma)
17-PMB-01 Hollywood	-119.0642	34.0903	5	Lower Topanga	Early- to Middle-Miocene	6.5 ± 0.4	
17-HW-09	-118.3425	34.1283	294	Upper Topanga	Middle-Miocene	6.8 – 44.1 ^{a,b}	

Note. Thermochronometry data assessment and rejection criteria is identical to Table 1.

^aMean cooling age is older than the depositional age of the sedimentary rock. Range of grain ages reported instead of mean age. ^bStandard error is >20% of mean age. Range of grain ages reported instead of mean age. ^cAll but one grain rejected due to <5 ppm U concentration. Mean age not reported. ^dLess than three grains analyzed or remaining after rejecting outliers and low-U grains. Range of grain ages reported instead of mean age.

Samples both on and off transects yield mean ZHe cooling ages that range from 15 to 56 Ma. Samples collected from stratigraphic units that are middle-Eocene or older yield reset ZHe cooling ages. However, ZHe cooling ages that are considerably older than AHe cooling ages from the same sample suggests that these samples were variably thermally reset within the ZHe partial retention zone. Samples from stratigraphic units that are late-Eocene and younger yield ZHe cooling ages that are the same as, or older than, the depositional ages of the sedimentary rocks from which they were collected. We infer that these samples were not thermally reset during burial and therefore do not record cooling related to post-depositional exhumation.

4.1. Santa Ynez Mountains

We collected samples for AHe and ZHe thermochronometry along Rattlesnake Canyon, north of Santa Barbara, CA, and along Matilija Canyon north of Ojai, CA (Figure 3a). These transects are above the blind section of the San Cayetano Fault and within the inferred hanging wall of the near-vertical Santa Ynez Fault. The Rattlesnake Canyon transect includes three samples that span 2,100 m of stratigraphic separation in Cretaceous through Oligocene sandstones (Dibblee & Ehrenspeck, 1986). AHe ages range from 2.0 to 3.8 Ma, and ZHe analyses from the stratigraphically lowest sample (18-SBRC-07) yield a mean age of 15.3 ± 0.6 Ma (Table 1). The Matilija Canyon transect includes six samples that span 3,500 m of stratigraphic separation in Cretaceous through Oligocene sandstones (Dibblee, 1985, 1987a). AHe ages range from 1.6 to 2.9 Ma, and ZHe analyses on five samples yield mean ages of 17.7–35.3 Ma (Table 1). A ZHe cooling age from one additional sample (17-OJ-01) exceeds the depositional age of the sampled Oligocene strata. Additionally, White (1992) reported a mean apatite fission track age of 2.0 ± 1.2 Ma (WG2-90) from a sample collected from the same outcrop as 17-OJ-07 (AHe age of 2.0 Ma). The mean age and track lengths of sample WG2-90 were incorporated into the thermal models. AHe and ZHe analyses on both transects demonstrate clear age-stratigraphic relationships, but no age-elevation trend (Table 1, Table S1 in Supporting Information S1).

4.2. Topatopa Mountains

We collected samples for AHe and ZHe thermochronology along five transects in the Topatopa Mountains, including, from west to east, Sisar Canyon northeast of Ojai, CA, Santa Paula Canyon and Santa Paula Peak north of Santa Paula, CA, Hopper Mountain north of Fillmore, CA, and Piru Canyon north of Piru, CA (Figure 3a). All transects are in the hanging wall of the emergent section of the San Cayetano Fault, and AHe cooling ages from Eocene through lower-Miocene strata range from 2.1 to 3.4 Ma in the western transects, to 1.3–3.3 Ma in the eastern transects. ZHe cooling ages from Eocene strata are 27–56 Ma, but ZHe cooling ages from Oligocene and Miocene strata are older than depositional ages of the sampled strata. Stratigraphic separation across the San Cayetano Fault decreases from west to east, as does the stratigraphic age of units exposed in the hanging wall (Rockwell, 1988). AHe cooling ages from samples collected from middle-upper Miocene strata along the easternmost transect at Piru are variably reset. For AHe samples that were fully reset on the Piru transect, we were unable to solve for unique time-temperature histories with thermal history modeling due to the lack of stratigraphic or elevation separation between samples. AHe and ZHe data from one sample were used to produce the Santa Paula Canyon thermal model, so no elevation or stratigraphic

separation information was incorporated. Cooling ages from the Sisar Canyon, Santa Paula Peak, and Hopper Mountain transects show systematic age-elevation relationships.

4.3. Santa Monica Mountains and Northern Channel Islands

Samples were collected along one transect in the easternmost Santa Monica Mountains (Hollywood) (Figure 3b). AHe cooling ages from a Cretaceous quartz diorite and nonconformably overlying Cretaceous sandstone at the base of the Hollywood transect range from 2.6 to 8.6 Ma (Table 1). ZHe analyses from the lowest sample on the transect yield a mean cooling age of 20.6 Ma (Table 1). The Cretaceous sandstone is disconformably overlain by Miocene strata, and AHe cooling ages of 7.1–8.7 Ma from three samples collected from Middle-Miocene units are within the depositional age range of the sampled strata. These samples were included in the thermal model for predicted time-temperature histories but were not included in the inverse modeling for the best-fit thermal histories (Figure 4). One sample on the Hollywood transect yielded a cooling age older than the depositional age of the sampled strata (Table 2).

Samples were collected along two transects in the northern Channel Islands (Figure 3b). On Santa Rosa Island, five samples spanning 1,000 m of stratigraphic separation across Eocene through Miocene strata yield AHe ages of 6.4–9.6 Ma. A sixth sample from overlying Miocene strata yielded grain ages that exceed the depositional age of the formation. ZHe analyses from the stratigraphically lowest sample yield grain ages ranging from 51 to 85 Ma, which are older than the Middle-Eocene depositional age of the formation. On Santa Cruz Island, AHe cooling ages of seven samples from Paleocene through Miocene sedimentary rocks do not exhibit a systematic age-stratigraphic depth or age-elevation relationships. AHe analyses from one sample (18-PS-03) yield a relatively young cooling age of 7.0 ± 0.6 Ma, which is consistent with cooling ages from Santa Rosa Island (Figure 3b, Tables 1 and 2). However, AHe cooling ages from three other samples are within or older than the depositional ages of the sampled Miocene strata, and AHe ages of three samples from Eocene and Paleocene strata yield variable cooling ages ranging from 18.2 to 29.5 Ma.

Previously published ages from the central Santa Monica mountains were reported by Niemi and Clark (2018) (Figure 3b). AHe and ZHe data were collected along Las Flores Canyon and Zuma Ridge spanning 1,600 m (Las Flores Canyon) and 900 m (Zuma Ridge) of stratigraphic separation. AHe ages from eight samples on the Las Flores Canyon transect range from 2.3 to 11.5 Ma, and AHe ages of 13 samples from Zuma Ridge range from 4.5 to 12.6 Ma. AHe ages exhibit both age-stratigraphic depth and age-elevation trends. ZHe ages from three samples on these transects range from 36 to 61 Ma.

5. Exhumation Histories From Thermal Models

Thermal history models were produced in QTQt and yield constraints on the timing and rates of cooling of rocks above individual faults. We infer that the thermal histories record burial histories followed by the initiation of exhumation (erosion), and rates of exhumation averaged over the last several million years caused by reverse faulting. Models generally reveal cooling initiating in late Miocene through Pliocene time and continuing to the present (Figures 4 and S4–S14 in Supporting Information S1). Full thermal histories are included in Text S3 and Figures S4–S14 in Supporting Information S1. Here we focus on the post-depositional exhumation history.

An implicit assumption of the thermal modeling approach is that the current vertical sample separation reflects the paleo-vertical separation as samples passed through the AHe and ZHe partial retention zones (Farley, 2002). In a rapidly evolving structural system like the WTR, or where fault geometry is listric (Seeber & Sorlien, 2000), rotation of structural blocks in the uppermost crust may change the vertical separation of samples between the time the block passed through the helium partial retention zones and its exhumation to the surface (Figure 5). We observe an inverse relationship between stratigraphic depth and cooling ages on the Rattlesnake Canyon and Matilija Canyon transects despite the near-vertical attitude of the strata today, suggesting that a component of the rotation occurred after the samples passed through the helium partial retention zone. For these transects, we modeled samples using vertical separation defined by both elevation and stratigraphic separation, but we found that for both cases, predicted AHe and ZHe ages poorly fit the observed data (Figures 5 and S4–S8 in Supporting Information S1). Samples on both transects were collected from a narrow elevation range, so defining the vertical sample separation using stratigraphic

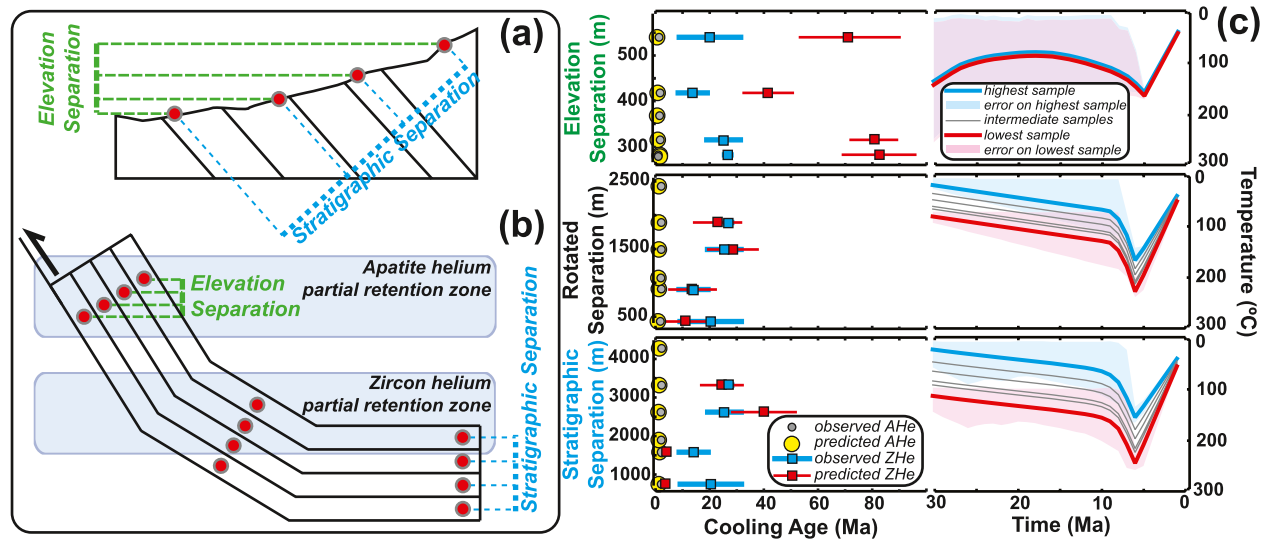


Figure 5. Schematic figures and cooling histories demonstrating the effect of changing vertical sample separation on transects. (a) Schematic cross section demonstrating the relative difference in vertical spacing between samples (red dots) on an individual transect depending on whether elevation or stratigraphic separation are used to define the distance between samples. (b) Rotation of strata in the hanging wall of a thrust ramp as sampled units pass through the apatite helium and zircon helium partial retention zones. Typically, the stratigraphically lowest sample is also the lowest elevation sample. (c) Inverse thermal modeling results for the Matilija Canyon transect (Figure 2), with observed and predicted apatite He and zircon He cooling ages (left) and best-fit thermal histories (right). Prior to running the inverse cooling models, vertical sample separation was defined using elevation in the upper model, using a 35° paleo-dip in the center model, and using stratigraphic separation in the lower model. Note that the stratigraphic section on the Matilija Canyon transect is overturned, and that the highest-elevation sample is also the stratigraphically lowest. Error bars are ranges of sampled Helium ages. Ranges of sampled apatite He ages are <2 Ma, and error bars are smaller than the AHe symbol size.

separation increases the spacing between samples as compared to elevation separation (Figure 5). We find that thermal models from these transects with vertical separation defined by stratigraphic separation underpredict ZHe ages from the lowest samples (Figures 5, S5 and S7 in Supporting Information S1). However, thermal models from these transects produced with vertical separation defined by elevation overpredict ZHe ages (Figures 5 and S8 in Supporting Information S1). Based on the results of end-member models with vertical sample separation defined using elevation or stratigraphic separation, and the near-vertical attitude of the strata that we sampled, we infer that the strata rotated from horizontal to vertical as they passed through the AHe and ZHe partial retention zones. We assess the orientation of the samples at the time of cooling through the partial retention zones by calculating sample separation for several possible paleo-orientation configurations. We find that reducing vertical sample separation by rotating the stratigraphic sections back 55° from the current near-vertical dip to a paleo-dip of ~35° results in thermal models with predicted AHe and ZHe ages that closely match observed ages (Figure 5). Rates of exhumation inferred from thermal models with vertical sample separation defined using the full stratigraphic separation and reduced vertical sample separation defined using the rotated sections differ by less than 10 percent, and the timing of cooling initiation is unchanged. We also note that the modeled ~35° paleo-dip is consistent with typical thrust ramp geometries.

Thermal modeling results reveal a gradient in the timing of cooling initiation along the San Cayetano Fault system. Cooling on the San Cayetano fault system first begins at ~8 Ma, as recorded by the Rattlesnake Canyon Transect (Table 2, Figure 4). At 6 Ma, cooling initiates at Matilija Canyon in the eastern Santa Ynez Mountains, at 5 Ma cooling initiates at Sisar Canyon at the boundary between the Santa Ynez Mountains and Topatopa Mountains, cooling initiates at 4 Ma at Santa Paula Canyon, and cooling initiates at 3 Ma at Santa Paula Peak and Hopper Mountain in the central to eastern Topatopa Mountains (Figure 4). Collectively, these data record cooling initiating first on the west end of the San Cayetano fault system and progressing eastward until at least ~3 Ma. Samples collected from the Miocene Modelo Formation at Piru Canyon at the eastern end of the Topatopa Mountains are variably reset for apatite, and therefore do not record a cooling age. However, the 3 Ma timing of exhumation inferred from the thermal models to the west at Hopper Mountain and Santa Paula Peak is consistent with an inferred ~3.2 Ma timing of initiation of the

San Cayetano Fault in the easternmost Topatopa Mountains (Levy et al., 2019; Rockwell, 1983). The timing of fault initiation is not constrained directly, but is inferred from microfauna analysis of the Lower Pliocene Pico Formation (Rockwell, 1983).

On the Santa Monica-Channel Islands fault system, the earliest cooling begins at ~10 Ma on Santa Rosa Island (Table 2, Figures 4 and 6). The timing of cooling is consistent with the end of deposition of the Beechers Bay Formation, the youngest sedimentary unit exposed on Santa Rosa Island today, in Middle Miocene time (Dibblee et al., 1998). Cooling initiates at 8 Ma at Zuma Ridge in the central Santa Monica Mountains, and at 5 Ma at Las Flores Canyon, which lies further to the east (Figures 4 and 6). Collectively, these data suggest cooling and inferred exhumation along the Santa Monica-Channel Islands fault system initiating first in the west and propagated east over ~5 million years (Figure 6). However, we acknowledge that the data density here is lower than in the north; sampling was limited by both the Pacific Ocean and the exposure of apatite-bearing sedimentary rocks that experienced sufficient burial to reset the apatite thermochronometer. Thermal history models from the Hollywood transect at the easternmost end of the Santa Monica Mountains imply cooling initiating between 7 and 8 Ma, earlier than cooling observed in the central portion of the range (Figures 4 and 6). The Santa Rosa Island, Zuma Ridge, and Las Flores Canyon cooling histories each experienced an initial phase of rapid cooling, followed by an apparent slower rate of cooling that continued until the present (Figure 4). However, the apparent decrease in cooling rate occurs at temperatures below the closure temperature of the AHe thermochronometer. The thermal histories are unconstrained at these low temperatures, and it is equally likely that no further cooling occurred after the initial pulse of rapid cooling (Figure 4), although marine terraces (Colson, 1996; Shaller & Heron, 2004) and geodetic data (Marshall et al., 2013) indicate Pleistocene to recent fault motion.

Time averaged rates of apparent exhumation (assuming a geothermal gradient of 30 °C/km) are generally higher on the San Cayetano fault system than on the Santa Monica-Channel Islands system (Figure 6 and Table 3). Exhumation rates along the six transects from Rattlesnake Canyon in the west, through Santa Paula Peak to the east range from 0.9 to 1.2 mm/yr. The Hopper Mountain transect to the east of Santa Paula Peak records a more rapid exhumation rate of 1.6 mm/yr. On the Santa Monica-Channel Islands fault system, Las Flores Canyon in the center of the range records the highest exhumation rate, at 1.0 mm/yr. Zuma Ridge records a slower exhumation rate of 0.7 mm/yr, and the Hollywood and Santa Rosa Island transects on the margins of the range record slower exhumation rates of 0.5 and 0.3 mm/yr, respectively (Table 3).

6. Discussion

The young cooling ages in the WTR can be contextualized within the regional tectonics by comparing these ages and rates to other fault bounded ranges adjacent to and surrounding the plate boundary. The regional distribution of cooling ages suggests that much of the rugged topography surrounding the Big Bend has experienced little exhumation in late Cenozoic time (Figure 1). Apatite fission track cooling ages from the San Rafael Mountains to the north of the WTR are early Miocene, Oligocene, and Eocene in age (White, 1992), and apatite fission track ages immediately south of the San Andreas Fault near Mt. Pinos are early-Miocene and Oligocene (Niemi et al., 2013) (Figure 1). AHe cooling ages from the northern San Gabriel Mountains generally exceed 10 Ma and are as old as Cretaceous (Buscher & Spotila, 2007). In contrast, the youngest ages recorded in WTR transects are latest Miocene through Quaternary, which are similar to ages in mountain ranges immediately adjacent to the San Andreas Fault, including the southeastern San Gabriel Mountains (AHe as young as ~1.8 Ma; Blythe et al., 2000), San Emigdio Mountains (AHe as young as 5 Ma; Niemi et al., 2013), and Yucaipa Ridge (AHe ages as young as 1.4 Ma; Spotila et al., 2001). The observation that thermochronometry ages from the WTR are similar in age or younger than ages much more proximal to the plate boundary indicates either a far more complex deformation field surrounding the Big Bend than previously envisioned by flower structures, or perhaps a structural distinction between the faults that underlie the WTR and the main plate boundary.

6.1. Initiation and Propagation of Reverse Faulting Within the Western Transverse Ranges

It has been previously assumed that the formation of the Big Bend geometry of the San Andreas Fault caused regional shortening within the surrounding area (Crowell, 1979, 1982; Link, 1982; Link & Osborne, 1978).

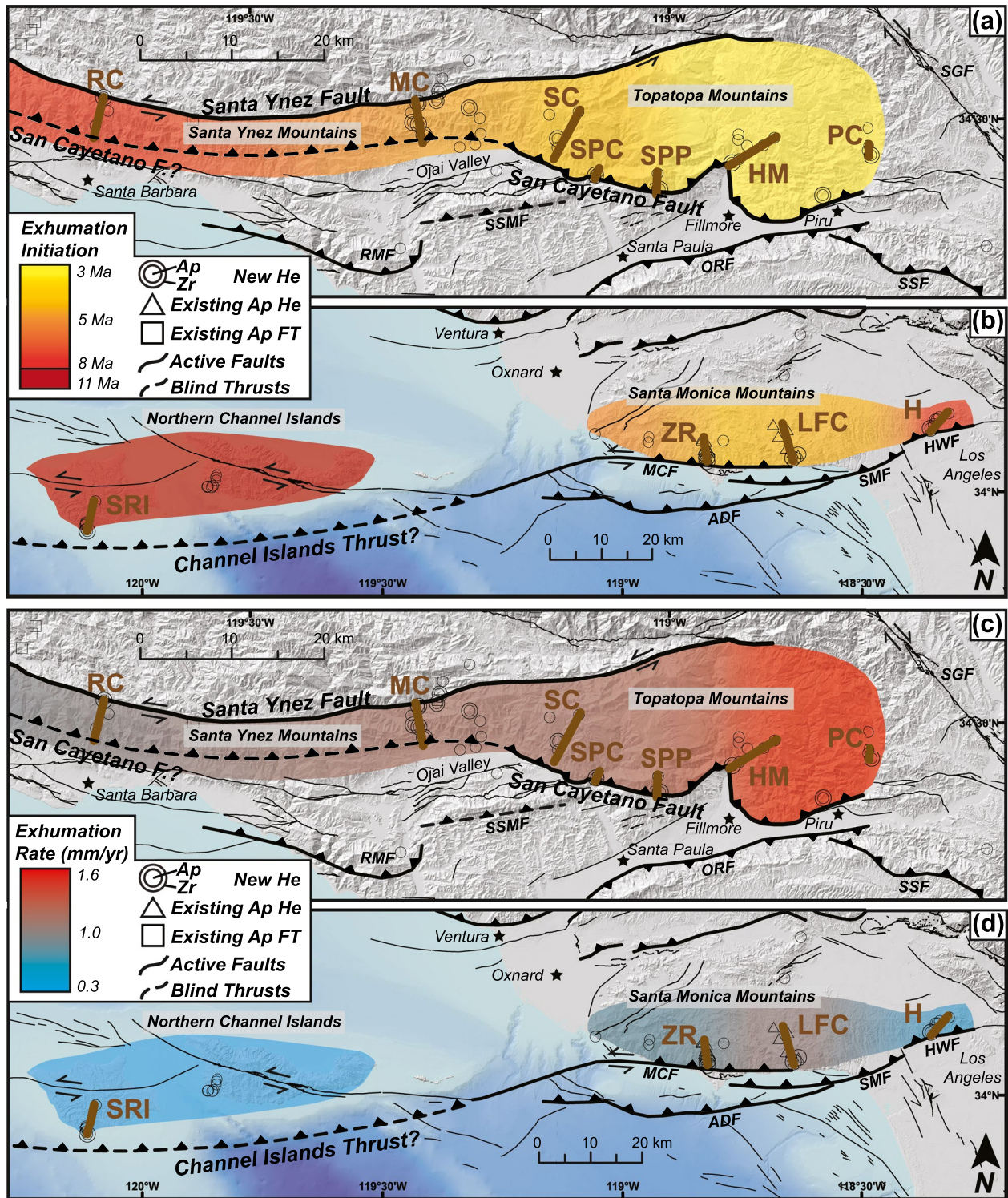


Figure 6. Timing of exhumation initiation along the (a) San Cayetano fault system, and (b) Santa Monica-Channel Islands fault system. (c) and (d) show apparent exhumation rates as inferred from the thermal models, assuming a geothermal gradient of 30°C/km. Panels (c) and (d) are the same extent as (a) and (b), respectively. Transect labels: RC—Rattlesnake Canyon; MC—Matilija Canyon; SC—Sisar Canyon; SPC—Santa Paula Canyon; SPP—Santa Paula Peak; HM—Hopper Mountain; PC—Piru Canyon; SRI—Santa Rosa Island; ZR—Zuma Ridge (Niemi & Clark, 2018); LFC—Las Flores Canyon (Niemi & Clark, 2018); H—Hollywood. Fault abbreviations: ADF—Anacapa-Dume Fault; HWF—Hollywood Fault; MCF—Malibu Coast Fault; ORF—Oak Ridge Fault; RMF—Red Mountain Fault; SGF—San Gabriel Fault; SMF—Santa Monica Fault; SSM—South Sulphur Mountain Fault; SSF—Santa Susana Fault.

Table 3
Timing of Exhumation Initiation and Average Exhumation Rates as Inferred From Thermal Models

Transect	Deepest strata exhumed	Timing of exhumation initiation (Ma)	Rate of exhumation (mm/yr)
San Cayetano fault system			
Rattlesnake Canyon	Cretaceous	8.0	0.9
Matilija Canyon	Cretaceous	6.0	1.2
Sisar Canyon	Early- to Middle-Eocene	5.0	1.2
Santa Paula Canyon	Late-Eocene	4.0	1.0
Santa Paula Peak	Middle- to Late- Eocene	3.0	1.2
Hopper Mountain	Oligocene	2.7	1.6
Santa Monica-Channel Islands fault system			
Santa Rosa Island	Middle-Eocene	10.0	0.3
Zuma Ridge	Paleocene	8.0	0.7
Las Flores Canyon	Upper Cretaceous	5.0	1.0
Hollywood	Cretaceous (pluton)	7.0	0.5

From that perspective, we could anticipate that (a) reverse faults would initiate synchronously with the initiation of the Big Bend at ~ 5 Ma, and (b) that reverse faults would propagate away from the San Andreas Fault Zone (i.e., east to west). However, our inferred fault histories challenge this assumed relationship, based on both the timing of fault initiation and the propagation directions of the major fault systems. For both the northern and southern WTR, we observe initial faulting in the west and prior to the formation of the Big Bend at ~ 5 Ma, with propagation of major fault systems toward the east over several million years.

The initiation of rock exhumation beneath the Santa Ynez and Topatopa Mountains starts at ~ 8 Ma and continues through 3 Ma (Figure 6). We suggest that this ~ 5 million year progression reflects the initiation and linkage of faults within the San Cayetano fault system (e.g., Abbey & Niemi, 2018), likely driven by eastward tip propagation of the San Cayetano Fault that underlies the Santa Ynez Mountains and becomes emergent in the Topatopa Mountains (Levy et al., 2019). The North Channel-Pitas Point and Ventura Fault trend similarly demonstrates a west-to-east propagation of reverse faulting and folding (Figure 3a; Hughes et al., 2018; Levy et al., 2019; Rockwell et al., 1984; Sorlien & Nicholson, 2015), although this fault trend is considerably younger than the principal fault systems on the boundaries of the WTR block, having likely initiated at ~ 1 Ma as a forward step in the San Cayetano fold-and-thrust belt system (Levy et al., 2019). The west to east propagation of faulting also mirrors the gradient in stratigraphic age of the sedimentary rocks exposed in the hanging wall of the fault, where Cretaceous strata are exposed in the west and Plio-Pleistocene sediments are exposed in the east (Dibblee, 1982). As the Topatopa Mountains contain a near-continuous sedimentary section, we infer that the stratigraphic age of exposed section is a crude proxy for the magnitude of exhumation, although we note that deposition in the easternmost part of the range was still ongoing when exhumation initiated in the west (Figure 8). The difference in the magnitude of exhumation along-strike is therefore likely a consequence of eastward-propagation of the San Cayetano Fault.

Exhumation initiates in the Santa Monica-Channel Islands fault system in the northern Channel Islands at ~ 10 Ma, followed by Zuma Ridge in the central Santa Monica Mountains at ~ 7 Ma, and Las Flores Canyon further to the east at 5 Ma (Niemi & Clark, 2018) (Figure 6). The Santa Monica-Channel Islands system is composed of a series of vertical sinistral and north-dipping thrusts that are argued to be part of regional, although segmented, thrust fault system, rather than a single through going fault (Davis & Namson, 1994; Seeber & Sorlien, 2000; Shaw & Suppe, 1994; Sorlien et al., 2006). Our data imply a ~ 5 million year eastward progression in the initiation of these individual structures, starting with the Channel Islands Thrust (Pinter et al., 2003; Shaw & Suppe, 1994) in the west, to the Malibu Coast Fault and Santa Monica Fault in the central and eastern Santa Monica Mountains (Niemi & Clark, 2018). However, we also acknowledge that the thermal history model of the Hollywood transect data implies that reverse faulting here initiated at ~ 7 Ma, prior to reverse faulting in the central portion of the Santa Monica Mountains. The easternmost

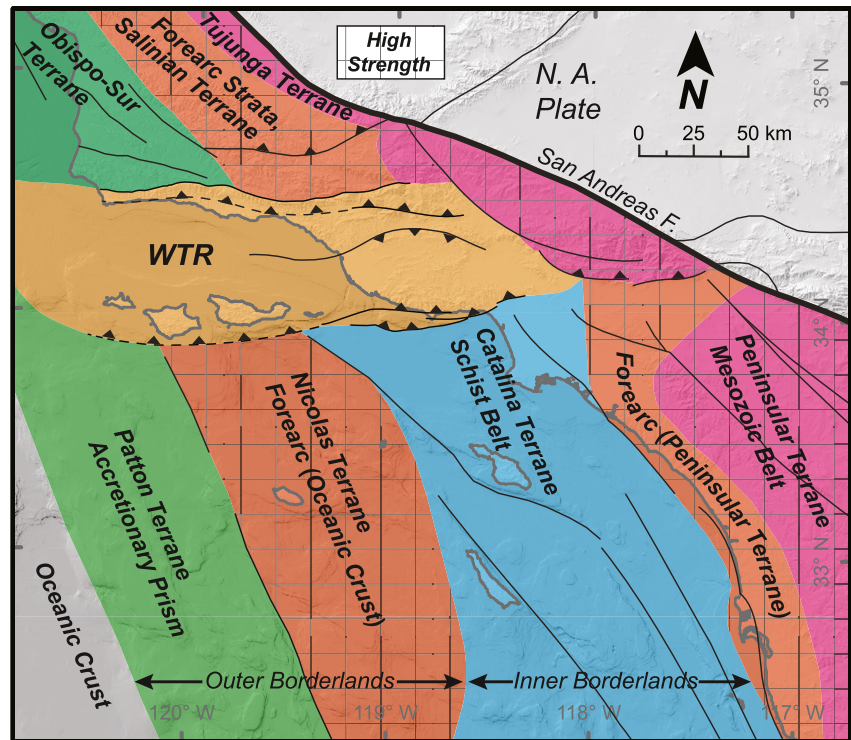


Figure 7. Generalized map of terranes and faults west of the Pacific-North American plate boundary in southern California. The east-west trending Western Transverse Ranges (WTR) are bounded to the north and south by northwest-southeast trending terranes of variable composition and lithospheric strength. The lithosphere-scale mechanical strength of the WTR is likely weaker than adjacent terranes due to its multi-stage history of rotation and extension. F–Fault; N. A., North American; Hatching shows terranes of relatively high lithospheric strength. Adapted from Bohannon and Geist (1998), Fisher et al. (2009), and M. Grove et al. (2008).

Santa Monica Mountains are at the extreme southeast corner of the WTR adjacent to the Verdugo Hills and San Gabriel Mountains, and exhumation initiation here may potentially be related to vertical motion on the San Gabriel Fault, the northern strand of which initiated at 7.5 Ma (Blythe et al., 2002).

Reverse faulting in the WTR is not likely to have initiated because of changes in strike of the plate boundary, at least initially. The Mojave Block on the east side of the San Andreas Fault has translated south relative to the Big Bend at a slower rate than the WTR have translated north relative to the bend. If we assume that the Mojave Block is fixed through time, restoration of slip across the San Andreas Fault places the WTR 300 km further south at 10 Ma, assuming a long-term slip rate of ~ 30 mm/yr (e.g., Figure 2; Crowell, 1979; Sieh & Jahns, 1984). At the time the Big Bend developed at 5 Ma, the WTR were located 150 km south of their current location, likely beyond the compressive stress field generated by the Big Bend. Therefore, initiation of strain localization within the WTR may be a manifestation of stresses unrelated to the restraining bend (e.g., Woodcock, 1986) and the current proximity of the WTR to the Big Bend is potentially a coincidence.

6.2. Regional Heterogeneities in Deformation and Rheology

We hypothesize that large-scale lithologic heterogeneities within the Pacific Plate play a role in localizing deformation within the WTR. The WTR are bounded to the north and south by a series of generally northwest- to southeast-striking terranes of variable composition and lithosphere-scale strength (Bohannon & Geist, 1998; Crouch, 1979; Crouch & Suppe, 1993; M. Grove et al., 2008; Reeves et al., 2015; ten Brink et al., 2000, Figure 7). South of the WTR, two of these terranes have relatively high lithosphere-scale strength, including the Nicolas Terrane and the Peninsular terrane. The Nicolas terrane lies south of Santa Cruz and Santa Rosa Islands and consists of more than three km of relatively undeformed Cretaceous through Oligocene forearc strata overlying oceanic crust (Crouch, 1979), while the Peninsular terrane is

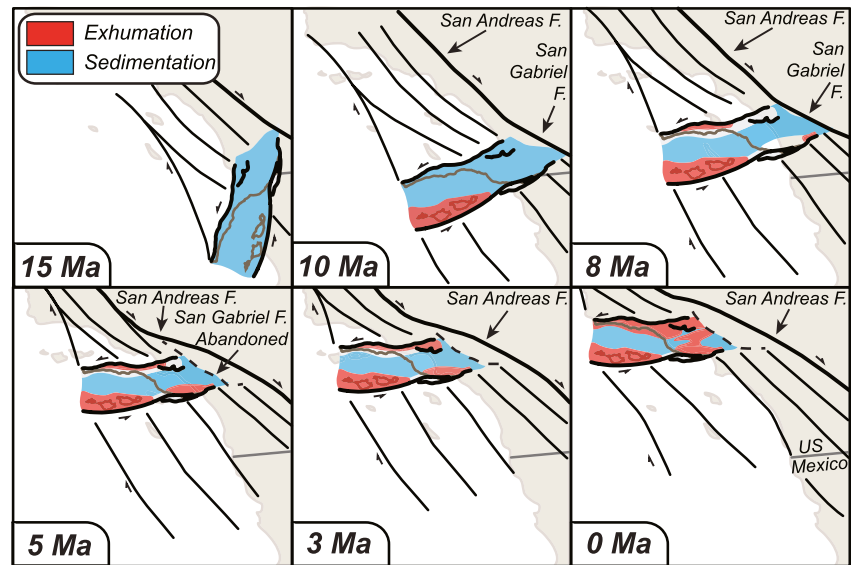


Figure 8. Time steps showing the rotation, sedimentation, and exhumation of the Western Transverse Ranges since 15 Ma. The modern coastline of southern California, USA and Baja California, Mexico, are shown for geographic context. Solid black lines are faults. Clockwise rotation of the Western Transverse Ranges (WTR) initiates between 16 and 14 Ma, and sedimentation occurs throughout the region under a predominantly transtensional tectonic regime. The first pulse of rock exhumation initiates at ~10 Ma on Santa Rosa Island as rotation, regional extension, and basin formation slows. At 8 Ma, cooling initiates in the Santa Ynez Mountains on the western end of the San Cayetano fault system as the WTR transitions from predominantly transtensional to transpressional. By 5–6 Ma, the San Gabriel Fault is abandoned as the main plate boundary structure as the southern San Andreas Fault forms to the east, creating the Big Bend restraining bend. By this time, reverse faulting on the Santa Monica–Channel Islands fault system has propagated east to the central Santa Monica Mountains, and reverse faulting on the San Cayetano fault system has propagated east into the Topatopa Mountains. By 3 Ma, exhumation across the Santa Monica–Channel Islands fault system has slowed, whereas exhumation on the San Cayetano fault system has continued propagating east. From 3 Ma to the present, forward propagation of the San Cayetano fold and thrust belt system results in rock exhumation in the center of the WTR block between the Santa Monica Mountains and Topatopa Mountains.

southeast of the Santa Monica Mountains and consists of relatively undeformed Mesozoic arc rocks overlain by forearc sedimentary strata (Crouch, 1979; Reeves et al., 2015; ten Brink et al., 2000) (Figure 7). Relatively strong terranes to the north of the WTR include the Precambrian-basement floored Tujunga Terrane to the northeast, and a thick sequence of Cretaceous–Cenozoic forearc sedimentary strata overlying Jurassic metasedimentary basement to the west (K. Grove, 1993; Kellog et al., 2008; Vedder et al., 1983). Thus, the WTR is juxtaposed between terranes to the north and south that have high lithospheric strength (Figure 7).

Forearc rocks of the WTR are underlain by pervasively sheared, mechanically weak Franciscan Complex rocks (Dibblee, 1982; Namson & Davis, 1988). Although the Franciscan Complex may also underlie other terranes to the north or south, the complicated history of extension, vertical-axis rotation, and subsequent shortening of the WTR potentially further weakened the underlying deep lithosphere of the block, compared to adjacent terranes (Figures 7 and 8; Atwater, 1998; Eymold & Jordan, 2019; Hornafius et al., 1986; Luyendyk, 1991). However, uncertainty remains over the deep lithospheric structure of the WTR; an upper-mantle high velocity body extending beneath the collective Transverse Ranges has been proposed to reflect downwelling of the Pacific Plate due to continent–continent collision (Fuis et al., 2012), but neither gravity nor receiver functions demonstrate measureable differences in the thickness of WTR lithosphere compared to other continental terranes (with the exception of the Inner Continental Borderlands, where the crust has thinned (Crouch, 1979; Lekic et al., 2011; Reeves et al., 2015; ten Brink et al., 2000).

We suggest that the contrasts in lithospheric strength of the adjacent terranes, as well as differential motions between the blocks, concentrate shortening within the WTR. The comparatively strong northwest–south–east trending lithospheric blocks on the Pacific Plate are translating to the northwest along the main plate boundary (Zeng & Shen, 2016), with the weak, extended, and rotated WTR caught in between. The

Miocene-to-present rotation of the WTR has also resulted in an orientation favorable to contraction, with the east-west fabric of the block juxtaposed against the northwest-southeast direction of plate motion. The potential differences in lithosphere-scale strength, and a favorable orientation for shortening, may explain the localization of deformation so far from the restraining bend in the main transform margin between the Pacific and North American plates.

Similarly, lithosphere-scale contrasts in rheology have been suggested to control the localization of deformation elsewhere along the Pacific-North American plate boundary (Niemi et al., 2013; Spotila et al., 2007; ten Brink et al., 2018; Zoback et al., 1987). Within the San Andreas Fault system, thermochronometry data from opposing sides of the transform margin reveal that Miocene to present deformation is localized within the weakened basement rocks of the San Emigdio Mountains (Niemi et al., 2013). This weak, deformed lithosphere is caught between comparatively strong Mesozoic Peninsular Ranges batholith and Proterozoic gneiss in the Mt. Pinos block to the south, and strong, dense oceanic lithosphere beneath the San Joaquin Valley to the north (Chapman et al., 2010; Holbrook & Mooney, 1987; Namson & Davis, 1988; Niemi et al., 2013). Niemi et al. (2013) hypothesize that these strong contrasts in the mechanical strength of the lithosphere played a role in localizing deformation within the weak lithosphere of the San Emigdio Mountains. A similar pattern is observed on the Queen Charlotte transform margin further north along the Pacific-North American plate boundary, where deformation localized on the boundary between continental and oceanic lithosphere (ten Brink et al., 2018).

The formation of the Big Bend itself is likely a consequence of lithosphere-scale contrasts in rheology. The location of the main strand of the Pacific-North American transform margin has stepped east through time, and the restraining bend developed with the opening of the Gulf of California and an eastward step of the southern San Andreas Fault into the deformed, weak basement of the Mojave Block (Atwater & Stock, 1998; Crowell, 1979; Oskin & Stock, 2003). The central segment of the San Andreas Fault is currently fixed on the western margin of the Sierran Microplate, where strong oceanic lithosphere and Sierran arc basement rocks likely explain a lack of observed internal deformation and prevent eastward stepping of the margin (Argus & Gordon, 1991; Plattner et al., 2010). The Big Bend is therefore required to transfer plate boundary motion from the eastward-stepping southern San Andreas Fault, around the mechanically strong Sierran Microplate to the central segment of the San Andreas, and ultimately north to the Mendocino Triple Junction.

Although the hypothesis that rheological contrasts may explain strain localization is not new (Niemi et al., 2013; Spotila et al., 2007; ten Brink et al., 2018; Zoback et al., 1987), our results from the WTR suggest that rheological contrasts may be more important to strain localization than proximity to restraining or releasing bends. The San Andreas Fault is the archetypal transform margin system from which new hypotheses are exported to other field settings, and detailed studies on dip-slip fault systems near other continental transform margins may reveal similarly complex fault initiation timing and propagation that challenge simple models of restraining- and releasing-bend tectonism.

7. Conclusions

Thermochronometric data from the WTR provide insight into the evolution of reverse faulting adjacent to the Big Bend restraining bend in the North American-Pacific Plate transform margin. High-density sampling for thermochronometric data from nine new transects and two published transects (Niemi & Clark, 2018) reveal predominantly Pliocene to Pleistocene apatite (U-Th-Sm)/He cooling ages along the San Cayetano fault system on the northern boundary of the WTR, and latest-Miocene to Pliocene cooling ages along the Santa Monica-Channel Islands fault system on the southern boundary. Cooling histories from inverse modeling of thermochronometry data imply an eastward propagation of reverse faulting over ~5 Myr on both fault systems. In the north, exhumation initiates in the Santa Ynez Mountains on the west end of the San Cayetano fault system at 8 Ma and progresses east until 3 Ma. In the south, exhumation first initiates in the northern Channel Islands at 10 Ma and propagates east to the central Santa Monica Mountains by 5 Ma. Along both boundaries, reverse faulting initiates prior to development of the Big Bend and propagates toward the San Andreas Fault, suggesting that restraining bend tectonism is not the primary source of shortening in the WTR as previously assumed. Post-Miocene deformation in the broader region around the Big Bend is localized within the WTR, which has mechanically weaker basement rocks. We posit

that contrasts in lithosphere-scale mechanical strength may explain the distribution of young cooling ages and active reserve faulting in the WTR. The hypothesis that rheological contrasts may be a more important control on strain localization than proximity to bends in continental transform margins, developed here from the San Andreas transform margin, has the potential to be exported broadly to other transform margin systems.

Data Availability Statement

Thermochronometry sample and analytical data are available at the University of Michigan Deep Blue data repository (<https://doi.org/10.7302/ab76-1628>).

Acknowledgments

This work was supported by a National Science Foundation division of Earth Science, Geomorphology and Land Use Dynamics award (EAR-1528576) to M. K. Clark and research grants from the Evolving Earth Foundation, the Geological Society of America, and the Department of Earth and Environmental Sciences at the University of Michigan to K. F. Townsend. We acknowledge the U.S. National Park Service and Forest Service for access and sample collection permits, and Salvador Dominguez, Tim Cohen (Rancho Temescal), Jim Lynn, Gordon Kimball, The Nature Conservancy, Seneca Resources, Carbon Energy Corporation, and Aera Energy for access to private or restricted properties. We thank Amanda Maslyn for laboratory support, Alyssa Abbey, Alexander Tye, and Nikolas Middtun for discussions and feedback on the thermal modelling methodology, and A. Joshua West, Nikolas Middtun, Bian Wang, Logan Knoper, William Medwedeff, Abra Atwood, Maxwell Dahlquist, and Eric Portenga for assistance in the field. We further thank James Spotila and one anonymous reviewer for detailed comments and suggestions that improved this manuscript.

References

- Abbey, A. L., & Niemi, N. A. (2018). Low-temperature thermochronometric constraints on fault initiation and growth in the northern Rio Grande rift, upper Arkansas River valley, Colorado, USA. *Geology*, *46*(7), 627–630. <https://doi.org/10.1130/G40232.1>
- Argus, D. F., & Gordon, R. G. (1991). Current Sierra Nevada-North America motion from very long baseline interferometry: Implications for the kinematics of the western United States. *Geology*, *19*(11), 1085–1088. [https://doi.org/10.1130/0091-7613\(1991\)019<1085:csnnam>2.3.co;2](https://doi.org/10.1130/0091-7613(1991)019<1085:csnnam>2.3.co;2)
- Armijo, R., Meyer, B., Hubert, A., & Barka, A. (1999). Westward propagation of the North Anatolian fault into the northern Aegean: Timing and kinematics. *Geology*, *27*(3), 267–270. [https://doi.org/10.1130/0091-7613\(1999\)027<0267:wpoatna>2.3.co;2](https://doi.org/10.1130/0091-7613(1999)027<0267:wpoatna>2.3.co;2)
- Armijo, R., Meyer, B., Navarro, S., King, G., & Barka, A. (2002). Asymmetric slip partitioning in the Sea of Marmara pull-apart: A clue to propagation processes of the North Anatolian Fault? *Terra Nova*, *14*(2), 80–86. <https://doi.org/10.1046/j.1365-3121.2002.00397.x>
- Atwater, T. (1998). Plate tectonic history of southern California with emphasis on the western Transverse Ranges and northern Channel Islands. In P. W. Weigand (Ed.), *Contributions to the geology of the Northern Channel Islands, southern California* (pp. 1–8). American Association of Petroleum Geologists. <https://doi.org/10.32375/1998-mp45.1>
- Atwater, T., & Stock, J. (1998). Pacific-North America plate tectonics of the Neogene Southwestern United States: An update. *International Geology Review*, *40*(5), 375–402. <https://doi.org/10.1080/00206819809465216>
- Blythe, A. E., Burbank, D. W., Farley, K. A., & Fielding, E. J. (2000). Structural and topographic evolution of the central transverse ranges, California, from apatite fission-track, (U-Th)/He and digital elevation model analyses. *Basin Research*, *12*(2), 97–114. <https://doi.org/10.1046/j.1365-2117.2000.00116.x>
- Blythe, A. E., House, M. A., & Spotila, J. A. (2002). Low-temperature thermochronology of the San Gabriel and San Bernardino Mountains, Southern California; constraining structural evolution. *Special Paper - Geological Society of America*, *365*, 231–250. <https://doi.org/10.1130/0-8137-2365-5.231>
- Bohannon, R. G., & Geist, E. (1998). Upper crustal structure and Neogene tectonic development of the California continental borderland. *The Geological Society of America Bulletin*, *110*(6), 779–800. [https://doi.org/10.1130/0016-7606\(1998\)110<0779:uacsant>2.3.co;2](https://doi.org/10.1130/0016-7606(1998)110<0779:uacsant>2.3.co;2)
- Bostick, N. H., Cashman, S. M., McCulloh, T. H., & Waddell, C. T., (1978). Gradients of vitrinite reflectance and present temperature in the Los Angeles and Ventura basins. In D. F. Oltz (Ed.), *Symposium in geochemistry: Low temperature metamorphism of Kerogen and clay minerals* (pp. 65–96). Pacific Section of the Society of Economic Paleontology and Mineralogy.
- Buscher, J. T., & Spotila, J. A. (2007). Near-field response to transpression along the southern San Andreas fault, based on exhumation of the northern San Gabriel Mountains, southern California. *Tectonics*, *26*(5), 1–15. <https://doi.org/10.1029/2006TC002017>
- Chapman, A. D., Kidder, S., Saleeby, J. B., & Ducea, M. N. (2010). Role of extrusion of the Rand and Sierra de Salinas schists in Late Cretaceous extension and rotation of the southern Sierra Nevada and vicinity. *Tectonics*, *29*(5), 1–21. <https://doi.org/10.1029/2009TC002597>
- Collett, C. M., Duvall, A. R., Flowers, R. M., Tucker, G. E., & Upton, P. (2019). The timing and style of oblique deformation within New Zealand's Kaikōura Ranges and Marlborough Fault System based on low-temperature thermochronology. *Tectonics*, *38*, 1–23. <https://doi.org/10.1029/2018TC005268>
- Colson, K. B. (1996). *Neotectonics of the left-lateral Santa Rosa Island Fault, western Transverse Ranges, southern California* (M.S. Thesis). San Diego State University.
- Cooke, M. L., Schottenfeld, M. T., & Buchanan, S. W. (2013). Evolution of fault efficiency at restraining bends within wet kaolin analog experiments. *Journal of Structural Geology*, *51*, 180–192. <https://doi.org/10.1016/j.jsg.2013.01.010>
- Cooke, M. L., Toeneboehn, K., & Hatch, J. L. (2020). Onset of slip partitioning under oblique convergence within scaled physical experiments. *Geosphere*, *16*(3), 875–889. <https://doi.org/10.1130/ges02179.1>
- Cowan, H., Nicol, A., & Tonkin, P. (1996). A comparison of historical and paleoseismicity in a newly formed fault zone and a mature fault zone, North Canterbury, New Zealand. *Journal of Geophysical Research*, *101*(3), 6021–6036. <https://doi.org/10.1029/95jb01588>
- Crouch, J. K. (1979). Neogene tectonic evolution of the California Continental Borderland and western Transverse Ranges. *Bulletin of the Geological Society of America*, *90*(4), 338–345. [https://doi.org/10.1130/0016-7606\(1979\)90<338:mteotc>2.0.co;2](https://doi.org/10.1130/0016-7606(1979)90<338:mteotc>2.0.co;2)
- Crouch, J. K., & Suppe, J. (1993). Late Cenozoic tectonic evolution of the Los Angeles Basin and inner California borderland: A model for core complex-like crustal extension. *The Geological Society of America Bulletin*, *105*(11), 1415–1434. [https://doi.org/10.1130/0016-7606\(1993\)105<1415:lctecot>2.3.co;2](https://doi.org/10.1130/0016-7606(1993)105<1415:lctecot>2.3.co;2)
- Crowell, J. C. (1979). The San Andreas fault system through time. *Journal of the Geological Society*, *136*, 293–302. <https://doi.org/10.1144/gsjgs.136.3.0293>
- Crowell, J. C. (1982). The tectonics of Ridge Basin, southern California. In J. C. Crowell, & M. H. Link (Eds.), *Geologic history of Ridge Basin, southern California* (pp. 25–42). Pacific Section, Society of Economic Paleontologists and Mineralogists.
- Cunningham, W. D., & Mann, P. (2007). Tectonics of strike-slip restraining and releasing bends. *Geological Society, London, Special Publications*, *290*, 1–12. <https://doi.org/10.1144/SP290.1>
- Darrow, A. C., & Sylvester, A. G. (1984). *Activity of the central reach of the Santa Ynez Fault: Continuation of investigations*. U.S. Geological Survey Technical Report. Contract 21367.
- Davis, T. L., & Namson, J. S. (1994). A balanced cross-section of the 1994 Northridge earthquake, southern California. *Nature*, *372*, 167–169. <https://doi.org/10.1038/372167a0>

- DeVecchio, D. E., Heermance, R. V., Fuchs, M., & Owen, L. A. (2012). Climate-controlled landscape evolution in the western Transverse Ranges, California: Insights from Quaternary geochronology of the Saugus Formation and strath terrace flights. *Lithosphere*, 4, 110–130. <https://doi.org/10.1130/L176.1>
- Dewey, J., Holdsworth, R., & Strachan, R. A. (1998). Transpression and transtension zones. In R. Holdsworth, R. A. Strachan, & J. F. Dewey (Eds.), *Continental transpressional and transtensional tectonics* (Vol. 135, pp. 1–14). Geological Society, London, Special Publications. <https://doi.org/10.1144/gsl.sp.1998.135.01.01>
- Dibblee, T. W. (1982). Regional geology of the Transverse Ranges Province of southern California. In D. L. Fefe, & J. A. Minch (Eds.), *Geology and mineral wealth of the California Transverse ranges* (pp. 7–26). South Coast Geological Society, Inc.
- Dibblee, T. W. (1985). *Geologic map of the Wheeler Springs quadrangle, Ventura county, California*. Dibblee Geological Foundation.
- Dibblee, T. W. (1987a). *Geologic map of the Matilija quadrangle, Ventura county, California*. Dibblee Geological Foundation.
- Dibblee, T. W. (1987b). *Geologic map of the Ojai quadrangle, Ventura county, California*. Dibblee Geological Foundation.
- Dibblee, T. W. (1990a). *Geologic map of the Fillmore quadrangle*. Dibblee Geological Foundation.
- Dibblee, T. W. (1990b). *Geologic map of the Santa Paula Peak quadrangle*. Dibblee Geological Foundation.
- Dibblee, T. W. (1991a). *Geologic map of the Beverly Hills and south 1/2 Van Nuys quadrangles*. Dibblee Geological Foundation.
- Dibblee, T. W. (1991b). *Geologic map of the Hollywood and south 1/2 Burbank quadrangles*. Dibblee Geological Foundation.
- Dibblee, T. W. (1991c). *Geologic map of the Piru quadrangle, Ventura county, California*. Dibblee Geological Foundation.
- Dibblee, T. W., & Ehrenspeck, H. E. (1986). *Geologic map of the Santa Barbara quadrangle, Santa Barbara county, California*. Dibblee Geological Foundation.
- Dibblee, T. W., & Ehrenspeck, H. E. (1997). *Geologic map of the Whitaker Peak quadrangle, Los Angeles and Ventura counties*. Dibblee Geological Foundation.
- Dibblee, T. W., Woodley, J. J., & Ehrenspeck, H. E. (1998). *Geologic map of the Santa Rosa Island quadrangle, Santa Barbara county, California*. Dibblee Geological Foundation.
- Dickinson, W. R. (1996). Kinematics of transrotational tectonism in the California transverse ranges and its contribution to cumulative slip along the San Andreas transform fault system. *Special Paper of the Geological Society of America*, 305. <https://doi.org/10.1130/0-8137-2305-1.1>
- Dolan, J. F., & Pratt, T. L. (1997). High-resolution seismic reflection profiling of the Santa Monica Fault Zone, West Los Angeles, California. *Geophysical Research Letters*, 24(16), 2051–2054. <https://doi.org/10.1029/97gl01940>
- Dolan, J. F., Sieh, K., & Rockwell, T. K. (2000). Late quaternary activity and seismic potential of the Santa Monica fault system, Los Angeles, California. *Bulletin of the Geological Society of America*, 112(10), 1559–1581. [https://doi.org/10.1130/0016-7606\(2000\)112<1559:lqaasp>2.0.co;2](https://doi.org/10.1130/0016-7606(2000)112<1559:lqaasp>2.0.co;2)
- Dolan, J. F., Sieh, K., Rockwell, T. K., Gupta, P., & Miller, G. (1997). Active tectonics, paleoseismology, and seismic hazards of the Hollywood fault, northern Los Angeles basin, California. *Bulletin of the Geological Society of America*, 109(12), 1595–1616. [https://doi.org/10.1130/0016-7606\(1997\)109<1595:atpash>2.3.co;2](https://doi.org/10.1130/0016-7606(1997)109<1595:atpash>2.3.co;2)
- Dolan, J. F., Sieh, K., Rockwell, T. K., Yeats, R. S., Shaw, J. H., Suppe, J., et al. (1995). Prospects for larger or more frequent Earthquakes in the Los Angeles Metropolitan Region. *Science*, 267(5195), 199–205. <https://doi.org/10.1126/science.267.5195.199>
- Duffy, B., Quigley, M., Barrell, D. J. A., Van Dissen, R., Stahl, T., Leprince, S., et al. (2013). Fault kinematics and surface deformation across a releasing bend during the 2010 MW 7.1 Darfield, New Zealand, earthquake revealed by differential LiDAR and cadastral surveying. *Bulletin of the Geological Society of America*, 125(3–4), 420–431. <https://doi.org/10.1130/B30753.1>
- Ehlers, T. A. (2005). Crustal thermal processes and the interpretation of thermochronometer data. *Reviews in Mineralogy and Geochemistry*, 58(1), 315–350. <https://doi.org/10.2138/rmg.2005.58.12>
- Ehlig, P. L., Ehlert, K. W., & Crowem, B. M. (1975). Offset of the upper Miocene Caliente and Mint Canyon formations along the San Gabriel and San Andreas faults. *California Division of Mines and Geology Special Report*, 118, 83–92.
- Eymold, W. K., & Jordan, T. H. (2019). Tectonic regionalization of the Southern California crust from tomographic cluster analysis. *Journal of Geophysical Research: Solid Earth*, 124(11), 11840–11865. <https://doi.org/10.1029/2019JB018423>
- Farley, K. A. (2002). (U-Th)/He dating: Techniques, calibrations, and applications. *Reviews in Mineralogy and Geochemistry*, 47(1), 819–844. <https://doi.org/10.2138/rmg.2002.47.18>
- Fisher, M. A., Langenheim, V. E., Nicholson, C., Ryan, H. F., & Sliter, R. W. (2009). Recent developments in understanding the tectonic evolution of the Southern California offshore area: Implications for earthquake-hazard analysis. *Special Papers - Geological Society of America*, 245(4), 229–250. [https://doi.org/10.1130/2009.245\(4.2\)](https://doi.org/10.1130/2009.245(4.2))
- Fuis, G. S., Scheirer, D. S., Langenheim, V. E., & Kohler, M. D. (2012). A new perspective on the geometry of the San Andreas fault in southern California and its relationship to Lithospheric structure. *Bulletin of the Seismological Society of America*, 102(1), 236–251. <https://doi.org/10.1785/0120110041>
- Gallagher, K. (2012). Transdimensional inverse thermal history modeling for quantitative thermochronology. *Journal of Geophysical Research*, 117(2), 1–16. <https://doi.org/10.1029/2011JB008825>
- Graham, S. A., Stanley, R. G., Bent, J. V., & Carter, J. B. (1989). Oligocene and Miocene paleogeography of central California and displacement along the San Andreas fault. *The Geological Society of America Bulletin*, 101(5), 711–730. [https://doi.org/10.1130/0016-7606\(1989\)101<0711:oampoc>2.3.co;2](https://doi.org/10.1130/0016-7606(1989)101<0711:oampoc>2.3.co;2)
- Grove, K. (1993). Latest Cretaceous basin formation within the Salinian terrane of west-central California. *The Geological Society of America Bulletin*, 105(4), 447–463. [https://doi.org/10.1130/0016-7606\(1993\)105<0447:lcbfw>2.3.co;2](https://doi.org/10.1130/0016-7606(1993)105<0447:lcbfw>2.3.co;2)
- Grove, M., Bebout, G. E., Jacobson, C. E., Barth, A. P., Kimbrough, D. L., King, R. L., et al. (2008). The Catalina Schist: Evidence for middle Cretaceous subduction erosion of southwestern North America. In A. E. Draut, P. D. Clift, & D. W. Scholl (Eds.), *Formation and applications of the sedimentary record in arc collision zones* (Vol. 436, pp. 335–361). The Geological Society of America Special Paper. [https://doi.org/10.1130/2008.2436\(15\)](https://doi.org/10.1130/2008.2436(15))
- Guenther, W. R., Reiners, P. W., Ketcham, R. A., Nasdala, L., & Giester, G. (2013). Helium diffusion in natural zircon: Radiation damage, anisotropy, and the interpretation of zircon (U-Th)/He thermochronology. *American Journal of Science*, 313(3), 145–198. <https://doi.org/10.2475/03.2013.01>
- Hatem, A. E., Cooke, M. L., & Madden, E. H. (2015). Evolving efficiency of restraining bends within wet kaolin analog experiments. *Journal of Geophysical Research: Solid Earth*, 120, 1975–1992. <https://doi.org/10.1002/2014JB011735>
- Hatem, A. E., Cooke, M. L., & Toeneboehn, K. (2017). Strain localization and evolving kinematic efficiency of initiating strike-slip faults within wet kaolin experiments. *Journal of Structural Geology*, 101, 96–108. <https://doi.org/10.1016/j.jsg.2017.06.011>
- Helmold, K. P., & van de Kamp, P. C. (1984). Diagenetic mineralogy and controls on albization and laumontite formation in Paleogene Arkoses, Santa Ynez Mountains, California. *AAPG Memoir*, 37(1), 239–276. <https://doi.org/10.1306/m37435c15>

- Hill, D. J. (1976). *Geology of the Jurassic Basement Rocks, Santa Cruz Island, California, and correlation with other mesozoic basement terranes in California* (pp. 16–46). American Association of Petroleum Geologists Pacific Section.
- Holbrook, W. S., & Mooney, W. D. (1987). The crustal structure of the axis of the Great Valley, California, from seismic refraction measurements. *Tectonophysics*, 140(1), 49–63. [https://doi.org/10.1016/0040-1951\(87\)90139-9](https://doi.org/10.1016/0040-1951(87)90139-9)
- Hornafius, J. S., Luyendyk, B. P., Terres, R. R., & Kamerling, M. J. (1986). Timing and extent of Neogene tectonic rotation in the western Transverse Ranges, California (USA). *The Geological Society of America Bulletin*, 97(12), 1476–1487. [https://doi.org/10.1130/0016-7606\(1986\)97<1476:taeont>2.0.co;2](https://doi.org/10.1130/0016-7606(1986)97<1476:taeont>2.0.co;2)
- Hubbard, J., Shaw, J. H., Dolan, J. F., Pratt, T. L., McAuliffe, L., & Rockwell, T. K. (2014). Structure and seismic hazard of the Ventura Avenue anticline and Ventura fault, California: Prospect for large, multisegment ruptures in the western Transverse Ranges. *Bulletin of the Seismological Society of America*, 104(3), 1070–1087. <https://doi.org/10.1785/0120130125>
- Huflite, G. J., & Yeats, R. S. (1996). Deformation rates across the Placerita (Northridge Mw = 6.7 Aftershock Zone) and Hopper Canyon segments of the western Transverse Ranges deformation belt. *Bulletin of the Seismological Society of America*, 86, 3–18.
- Hughes, A., Rood, D. H., Whittaker, A. C., Bell, R. E., Rockwell, T. K., Levy, Y., et al. (2018). Geomorphic evidence for the geometry and slip rate of a young, low-angle thrust fault: Implications for hazard assessment and fault interaction in complex tectonic environments. *Earth and Planetary Science Letters*, 504, 198–210. <https://doi.org/10.1016/j.epsl.2018.10.003>
- Jackson, J., & Molnar, P. (1990). Active faulting and block rotations in the western Transverse Ranges, California. *Journal of Geophysical Research*, 95(B13), 22073. <https://doi.org/10.1029/jb095ib13p22073>
- Kamerling, M. J., & Luyendyk, B. P. (1979). Tectonic rotations of the Santa Monica Mountains region, western Transverse Ranges, California, suggested by paleomagnetic vectors. *Bulletin of the Geological Society of America*, 90(4), 331–337. [https://doi.org/10.1130/0016-7606\(1979\)90<331:trotsm>2.0.co;2](https://doi.org/10.1130/0016-7606(1979)90<331:trotsm>2.0.co;2)
- Kamerling, M. J., & Luyendyk, B. P. (1985). Paleomagnetism and Neogene tectonics of the northern Channel Islands, California (USA). *Journal of Geophysical Research*, 90(B14), 12485–12502. <https://doi.org/10.1029/jb090ib14p12485>
- Kellog, K. S., Minor, S. A., & Cossette, P. M. (2008). Geologic Map of the Eastern Three-Quarters of the Cuyama 30' x 60' Quadrangle, California. *U.S. Geological Survey Scientific Investigations Map*, 3002, 23. <https://doi.org/10.3133/sim3002>
- Lekic, V., French, S. W., & Fischer, K. M. (2011). Lithospheric thinning beneath rifted regions of Southern California. *Science*, 334, 783–787. <https://doi.org/10.7551/mitpress/8876.003.0036>
- Levi, S., & Yeats, R. S. (1993). Paleomagnetic constraints on the initiation of uplift on the Santa Susana Fault, western Transverse Ranges, California. *Journal of Geophysical Research*, 98(B3), 688–702. <https://doi.org/10.1029/93tc00133>
- Levy, Y., Rockwell, T. K., Shaw, J. H., Plesch, A., Driscoll, N. W., & Perea, H. (2019). Structural modeling of the western Transverse Ranges: An imbricated thrust ramp architecture. *Lithosphere*, 1–38. <https://doi.org/10.1130/L1124.1>
- Link, M. H. (1982). Stratigraphic nomenclature and age of Miocene Strata, Ridge Basin, Southern California. In J. C. Crowell, & M. H. Link (Eds.), *Geologic history of Ridge Basin, southern California* (p. 5). Society of Economic Paleontologists and Mineralogists.
- Link, M. H., & Osborne, R. H. (1978). Lacustrine facies in the Pliocene Ridge Basin Group: Ridge Basin, California. In *Modern and Ancient Lake Sediments, Special Publication* (Vols. 169–187).
- Little, T. A., & Jones, A. (1998). Seven million years of strike-slip and related off-fault deformation, northeastern Marlborough fault system, South Island, New Zealand. *Tectonics*, 17(2), 285–302. <https://doi.org/10.1029/97tc03148>
- Lock, J., & Willett, S. (2008). Low-temperature thermochronometric ages in fold-and-thrust belts. *Tectonophysics*, 456, 147–162. <https://doi.org/10.1016/j.tecto.2008.03.007>
- Luyendyk, B. P. (1991). A model for Neogene crustal rotations, transtension, and transpression in southern California. *The Geological Society of America Bulletin*, 103(11), 1528–1536. [https://doi.org/10.1130/0016-7606\(1991\)103<1528:amfncr>2.3.co;2](https://doi.org/10.1130/0016-7606(1991)103<1528:amfncr>2.3.co;2)
- Luyendyk, B. P., Kamerling, M. J., & Terres, R. (1980). Geometric model for Neogene crustal rotations in southern California. *The Geological Society of America Bulletin*, 91(4), 211–217. [https://doi.org/10.1130/0016-7606\(1980\)91<211:gmfncr>2.0.co;2](https://doi.org/10.1130/0016-7606(1980)91<211:gmfncr>2.0.co;2)
- Madden, E. H., Cooke, M. L., & McBeck, J. A. (2017). Energy budget and propagation of faults via shearing and opening using work optimization. *Journal of Geophysical Research: Solid Earth*, 122(8), 6757–6772. <https://doi.org/10.1002/2017JB014237>
- Marshall, S. T., Funning, G. J., Krueger, H. E., Owen, S. E., & Loveless, J. P. (2017). Mechanical models favor a ramp geometry for the Ventura-pitas point fault, California. *Geophysical Research Letters*, 44, 1311–1319. <https://doi.org/10.1002/2016GL072289>
- Marshall, S. T., Funning, G. J., & Owen, S. E. (2013). Fault slip rates and interseismic deformation in the western Transverse Ranges, California. *Journal of Geophysical Research: Solid Earth*, 118(8), 4511–4534. <https://doi.org/10.1002/jgrb.50312>
- McAuliffe, L. J., Dolan, J. F., Rhodes, E. J., Hubbard, J., Shaw, J. H., & Pratt, T. L. (2015). Paleoseismologic evidence for large-magnitude (MW 7.5–8.0) earthquakes on the Ventura blind thrust fault: Implications for multifault ruptures in the Transverse Ranges of southern California. *Geosphere*, 11(5), 1629–1650. <https://doi.org/10.1130/GES01123.1>
- McBeck, J. A., Cooke, M., & Madden, E. (2017). Work optimization predicts the evolution of extensional step overs within anisotropic Host Rock: Implications for the San Pablo Bay, CA. *Tectonics*, 36(11), 2630–2646. <https://doi.org/10.1002/2017TC004782>
- McBeck, J. A., Madden, E. H., & Cooke, M. L. (2016). Growth by Optimization of Work (GROW): A new modeling tool that predicts fault growth through work minimization. *Computers & Geosciences*, 88, 142–151. <https://doi.org/10.1016/j.cageo.2015.12.019>
- McDowell, F. W., McIntosh, W. C., & Farley, K. A. (2005). A precise 40Ar–39Ar reference age for the Durango apatite (U-Th)/He and fission-track dating standard. *Chemical Geology*, 214(3–4), 249–263. <https://doi.org/10.1016/j.chemgeo.2004.10.002>
- Miller, F., & Morton, D. (1980). *Potassium-argon geochronology of the eastern Transverse ranges and southern Mojave Desert, southern California* (United States Geological Survey Professional Paper No. 1152, 1–30). <https://doi.org/10.3133/pp1152>
- Namson, J. S., & Davis, T. L. (1988). Structural transect of the western Transverse Ranges, California: Implications for lithospheric kinematics and seismic risk evaluation. *Geology*, 16, 675–679. [https://doi.org/10.1130/0091-7613\(1988\)016<0675:stotwt>2.3.co;2](https://doi.org/10.1130/0091-7613(1988)016<0675:stotwt>2.3.co;2)
- Nathenson, M., & Guffanti, M. (1987). *Compilation of geothermal-gradient data in the conterminous United States* (USGS Open-File Report 87-592, p. 33). U.S. Geological Survey. Retrieved from <https://pubs.usgs.gov/of/1987/0592/report.pdf>
- Nicholson, C., Sorlien, C. C., Atwater, T., Crowell, J. C., & Luyendyk, B. P. (1994). Microplate capture, rotation of the western Transverse Ranges, and initiation of the San Andreas transform as a low-angle fault system. *Geology*, 22(6), 491–495. [https://doi.org/10.1130/0091-7613\(1994\)022<0491:mcrotw>2.3.co;2](https://doi.org/10.1130/0091-7613(1994)022<0491:mcrotw>2.3.co;2)
- Niemi, N. A., Buscher, J. T., Spotila, J. A., House, M. A., & Kelley, S. A. (2013). Insights from low-temperature thermochronometry into transpressional deformation and crustal exhumation along the San Andreas fault in the western Transverse Ranges, California. *Tectonics*, 32(6), 1602–1622. <https://doi.org/10.1002/2013TC003377>
- Niemi, N. A., & Clark, M. K. (2018). Long-term exhumation rates exceed paleoseismic slip rates in the central Santa Monica Mountains, Los Angeles County, California. *Geology*, 46(1), 63–66. <https://doi.org/10.1130/G39388.1>

- Oskin, M., & Stock, J. (2003). Marine incursion synchronous with plate-boundary localization in the Gulf of California. *Geology*, *31*(1), 23–26. [https://doi.org/10.1130/0091-7613\(2003\)031<0023:miswpb>2.0.co;2](https://doi.org/10.1130/0091-7613(2003)031<0023:miswpb>2.0.co;2)
- Perea, H., Ucarukus, G., Driscoll, N. W., Kent, G. M., Levy, Y., & Rockwell, T. K. (2017). Holocene deformation events in the offshore Transverse Ranges (California, USA) constrained by new high-resolution geophysical data. In *Expanded abstract for the 8th International Union for Quaternary Research (INQUA) meeting on paleoseismology, active tectonics and archeoseismology (PATA)*, New Zealand (p. 4).
- Pinter, N., Johns, B., Little, B., & Vestal, W. D. (2001). Fault-related folding in California's Northern Channel Islands documented by rapid-static GPS positioning. *Geological Society of America Today*, *11*(5), 4–9. [https://doi.org/10.1130/1052-5173\(2001\)011<0004:frfnc>2.0.co;2](https://doi.org/10.1130/1052-5173(2001)011<0004:frfnc>2.0.co;2)
- Pinter, N., Sorlien, C. C., & Scott, A. T. (2003). Fault-related fold growth and isostatic subsidence, California Channel Islands. *American Journal of Science*, *303*(4), 300–318. <https://doi.org/10.2475/ajs.303.4.300>
- Plattner, C., Malservisi, R., Furlong, K. P., & Govers, R. (2010). Development of the Eastern California Shear Zone—Walker Lane belt: The effects of microplate motion and pre-existing weakness in the Basin and Range. *Tectonophysics*, *485*(1–4), 78–84. <https://doi.org/10.1016/j.tecto.2009.11.021>
- Quigley, M., Van Dissen, R., Litchfield, N., Villamor, P., Duffy, B., Barrell, D., et al. (2012). Surface rupture during the 2010 Mw 7.1 Darfield (Canterbury) earthquake: Implications for fault rupture dynamics and seismic-hazard analysis. *Geology*, *40*(1), 55–58. <https://doi.org/10.1130/G32528.1>
- Reeves, Z., Lelic, V., Schmerr, N., Kohler, M., & Weeraratne, D. (2015). Lithospheric structure across the California Continental Borderland from receiver functions. *Geochemistry, Geophysics, Geosystems*, *16*, 246–266. <https://doi.org/10.1002/2014GC005617>
- Reiners, P. W., Farley, K. A., & Hickey, H. J. (2002). He diffusion and (U-Th)/He thermochronometry of zircon: Initial results from Fish Canyon Tuff and Gold Butte. *Tectonophysics*, *349*(1–4), 297–308. [https://doi.org/10.1016/S0040-1951\(02\)00058-6](https://doi.org/10.1016/S0040-1951(02)00058-6)
- Reiners, P. W., & Nicolescu, S. (2006). Measurement of parent nuclides for (U-Th)/He chronometry by solution sector ICP-MS. In *ARDHL report 1* (pp. 1–33). Retrieved from <http://www.geo.arizona.edu/~reiners/ardhl/ardhl.html>
- Rockwell, T. K. (1983). *Soil chronology, geology, and neotectonics of the North Central Ventura Basin, California* (Ph.D dissertation). University of California Santa Barbara.
- Rockwell, T. K. (1988). Neotectonics of the San Cayetano fault, Transverse Ranges, California. *The Geological Society of America Bulletin*, *100*, 500–513. [https://doi.org/10.1130/0016-7606\(1988\)100<0500:motscf>2.3.co;2](https://doi.org/10.1130/0016-7606(1988)100<0500:motscf>2.3.co;2)
- Rockwell, T. K., Clark, K., Gamble, L., Oskin, M. E., Haaker, E. C., & Kennedy, G. L. (2016). Large Transverse range earthquakes cause coastal upheaval near Ventura, Southern California. *Bulletin of the Seismological Society of America*, *106*(6), 2706–2720. <https://doi.org/10.1785/0120150378>
- Rockwell, T. K., Keller, E. A., Clark, M. N., & Johnson, D. L. (1984). Chronology and rates of faulting of Ventura River terraces, California. *The Geological Society of America Bulletin*, *95*(12), 1466–1474. [https://doi.org/10.1130/0016-7606\(1984\)95<1466:carofo>2.0.co;2](https://doi.org/10.1130/0016-7606(1984)95<1466:carofo>2.0.co;2)
- Rohr, K. M. M. (2015). Plate boundary adjustments of the southernmost queen charlotte fault. *Bulletin of the Seismological Society of America*, *105*(2B), 1076–1089. <https://doi.org/10.1785/0120140162>
- Seeber, L., & Sorlien, C. C. (2000). Listric thrusts in the western Transverse Ranges, California. *Bulletin of the Geological Society of America*, *112*(7), 1067–1079. [https://doi.org/10.1130/0016-7606\(2000\)112<1067:ltitwt>2.0.co;2](https://doi.org/10.1130/0016-7606(2000)112<1067:ltitwt>2.0.co;2)
- Şengör, A. M. C., Tüysüz, O., Imren, C., Sakiç, M., Eyidoğan, H., Görür, N., et al. (2005). The North Anatolian Fault: A new look. *Annual Review of Earth and Planetary Sciences*, *33*, 37–112. <https://doi.org/10.1146/annurev.earth.32.101802.120415>
- Shaller, P. J., & Heron, C. W. (2004). Proposed revision of marine terrace extent, geometry, and rates of uplift, Pacific Palisades, California. *Environmental and Engineering Geoscience*, *10*(3), 253–275. <https://doi.org/10.2113/10.3.253>
- Shaw, J. H., & Suppe, J. (1994). Active faulting and growth folding in the eastern Santa Barbara Channel, California. *The Geological Society of America Bulletin*, *106*(5), 607–626. [https://doi.org/10.1130/0016-7606\(1994\)106<0607:AFAGFI>2.3.CO;2](https://doi.org/10.1130/0016-7606(1994)106<0607:AFAGFI>2.3.CO;2)
- Sieh, K. E., & Jahns, R. H. (1984). Holocene activity of the San Andreas fault at Wallace Creek, California. *The Geological Society of America Bulletin*, *8*, 883–896. [https://doi.org/10.1130/0016-7606\(1984\)95<883:haotsa>2.0.co;2](https://doi.org/10.1130/0016-7606(1984)95<883:haotsa>2.0.co;2)
- Sorensen, S. (1985). Petrologic evidence for Jurassic, island-arc-like basement rocks in the southwestern Transverse Ranges and California continental borderland. *The Geological Society of America Bulletin*, *96*(8), 997–1006. [https://doi.org/10.1130/0016-7606\(1985\)96<997:pefjib>2.0.co;2](https://doi.org/10.1130/0016-7606(1985)96<997:pefjib>2.0.co;2)
- Sorlien, C. C., Kamerling, M. J., Seeber, L., & Broderick, K. G. (2006). Restraining segments and reactivation of the Santa Monica-Dume-Malibu Coast fault system, offshore Los Angeles, California. *Journal of Geophysical Research*, *111*(11), 1–22. <https://doi.org/10.1029/2005JB003632>
- Sorlien, C. C., & Nicholson, C. (2015). Post-1 Ma deformation history of the Pitas Point-North Channel-Red Mountain Fault System and associated folds in Santa Barbara Channel, California. In *U.S. Geological Survey National Earthquake hazards reduction program final report, award G14AP00012, 1–24*.
- Spotila, J. A., Farley, K. A., Yule, J. D., & Reiners, P. W. (2001). Near-field transpressive deformation along the San Andreas fault zone in southern California, based on exhumation constrained by (U-Th)/He dating. *Journal of Geophysical Research*, *106*, 30909–30922. <https://doi.org/10.1029/2001JB000348>
- Spotila, J. A., Niemi, N., Brady, R., House, M., Buscher, J., & Oskin, M. (2007). Long-term continental deformation associated with transpressive plate motion: The San Andreas fault. *Geology*, *35*(11), 967–970. <https://doi.org/10.1130/G23816A.1>
- Stone, P. H., & Carlson, J. H. (1979). Atmospheric lapse rate regimes and their parameterization. *Journal of the Atmospheric Sciences*, *36*(3), 415–423. [https://doi.org/10.1175/1520-0469\(1979\)036<0415:alrrat>2.0.co;2](https://doi.org/10.1175/1520-0469(1979)036<0415:alrrat>2.0.co;2)
- ten Brink, U. S., Miller, N. C., Andrews, B. D., Brothers, D. S., & Haeussler, P. J. (2018). Deformation of the Pacific/North America Plate Boundary at Queen Charlotte Fault: The Possible Role of Rheology. *Journal of Geophysical Research: Solid Earth*, *123*(5), 4223–4242. <https://doi.org/10.1002/2017JB014770>
- ten Brink, U. S., Zhang, J., Brocher, T. M., Okaya, D. A., Klitgord, K. D., & Fuis, G. S. (2000). Geophysical evidence for the evolution of the California Inner Continental Borderland as a metamorphic core complex. *Journal of Geophysical Research*, *105*, 5835–5857. <https://doi.org/10.1029/1999jb900318>
- Teyssier, C., Tikoff, B., & Markley, M. (1995). Oblique plate motion and continental tectonics. *Geology*, *23*(5), 447–450. [https://doi.org/10.1130/0091-7613\(1995\)023<0447:opmact>2.3.co;2](https://doi.org/10.1130/0091-7613(1995)023<0447:opmact>2.3.co;2)
- Townsend, K. F., Gallen, S. F., & Clark, M. K. (2020). Quantifying near-surface rock strength on a regional scale from Hillslope Stability Models. *Journal of Geophysical Research: Earth Surface*, *125*(7). <https://doi.org/10.1029/2020JF005665>
- Vedder, J. G., Howell, D. G., & McLean, H. (1983). Stratigraphy, sedimentation, and tectonic accretion of exotic terranes, southern California Coast Ranges, California. *American Association of Petroleum Geologists Memoir*, *34*, 471–496. <https://doi.org/10.1306/M34430C25>

- Walcott, R. I. (1998). Modes of oblique compression: Late Cenozoic tectonics of the South Island of New Zealand. *Reviews of Geophysics*, 36(1), 1–26. <https://doi.org/10.1029/97RG03084>
- Wallace, L. M., Barnes, P., Beavan, J., Van Dissen, R., Litchfield, N., Mountjoy, J., et al. (2012). The kinematics of a transition from subduction to strike-slip: An example from the central New Zealand plate boundary. *Journal of Geophysical Research*, 117(2). <https://doi.org/10.1029/2011JB008640>
- White, L. (1992). *Thermal and unroofing history of the Western Transverse Ranges, California: Results from apatite fission track thermochronology* (Ph.D. dissertation). The University of Texas at Austin.
- Woodcock, N. H. (1986). The role of strike-slip fault systems at plate boundaries. *Philosophical Transactions of the Royal Society*, 317, 13–29. <https://doi.org/10.1098/rsta.1986.0021>
- Woodcock, N. H., & Fischer, M. (1986). Strike-slip duplexes. *Journal of Structural Geology*, 8(7), 725–735. [https://doi.org/10.1016/0191-8141\(86\)90021-0](https://doi.org/10.1016/0191-8141(86)90021-0)
- Wright, T. L. (1991). Structural geology and tectonic evolution of the Los Angeles Basin, California. In K. T. Biddle (Ed.), *Active margins basins* (Vol. 52, p. 35). American Association of Petroleum Geologists Memoir. <https://doi.org/10.1306/M52531C3>
- Yeats, R. S. (1981). Quaternary flake tectonics of the California Transverse Ranges. *Geology*, 9(1), 16–20. [https://doi.org/10.1130/0091-7613\(1981\)9<16:qfitot>2.0.co;2](https://doi.org/10.1130/0091-7613(1981)9<16:qfitot>2.0.co;2)
- Yeats, R. S. (1993). Converging more slowly. *Nature*, 366(6453), 299–301. <https://doi.org/10.1038/366299a0>
- Yerkes, R. F., & Lee, W. H. K. (1987). Late Quaternary deformation in the Western Transverse Ranges. In *Recent reverse faulting in the Transverse ranges*. U.S. Geological Survey. Professional Paper 1339.
- Zeng, Y., & Shen, Z. K. (2016). A fault-based model for crustal deformation, fault slip rates, and off-fault strain rate in California. *Bulletin of the Seismological Society of America*, 106(2), 766–784. <https://doi.org/10.1785/0120140250>
- Zoback, M., Lou, M. S., Van Mount, M. S., Suppe, J., Eaton, J. P., Healy, J. H., et al. (1987). New evidence on the state of stress of the San Andreas fault system. *Science*, 238(4830), 1105–1111. <https://doi.org/10.1126/science.238.4830.1105>

Reference From the Supporting Information

- Flowers, R. M., Ketcham, R. A., Shuster, D. L., & Farley, K. A. (2009). Apatite (U-Th)/He thermochronometry using a radiation damage accumulation and annealing model. *Geochimica et Cosmochimica Acta*, 73(8), 2347–2365. <https://doi.org/10.1016/j.gca.2009.01.015>